




Targeting *Msx2* as a brake in the fusion fate of osteoclasts and an anabolic therapy in pre-clinical models of osteoporosis

Received: 25 September 2024

Accepted: 3 July 2025

Published online: 06 August 2025

 Check for updates

Qingliang Ma^{1,2,3,8}, Shiyu Wang^{1,2,8}, Hong Xue^{1,2,4,8}, Linhui Ni⁵, Putao Yuan^{1,2}, Yang Shen^{1,2,6}, Bingjie Zheng^{1,2,6}, Qingqing Wang^{1,2}, Jiateng Zhang^{1,2}, Haoming Wang^{1,2}, Hongwei Xie^{1,2}, Chao Jiang^{1,2}, An Qin⁷, Shunwu Fan^{1,2} , Ziang Xie^{1,2}  & Zhiwei Jie^{1,2} 

Highly conserved homeobox genes are closely related to bone formation during embryogenesis, while their role in adult bone resorption remains unclear. In this study, we found that the homeobox gene *MSX2* actively participates bone metabolism. Myeloid-specific *Msx2* deficiency safeguards bone mass under physiological and pathological conditions. Loss of *Msx2* acts as a “brake” in the fusion fate of osteoclasts, resulting in a larger population of pre-osteoclasts. Pre-osteoclasts secrete platelet-derived growth factor-BB (PDGF-BB), which promotes angiogenesis-mediated bone formation. Mechanistically, *MSX2* directly binds to the vital osteoclastogenic transcription factor PU.1 and protects it from FBXW7-mediated ubiquitination degradation. *Msx2* and *Fbxw7* double knockout mitigated the protective effect of *MSX2* deficiency on bone mass. Finally, we identified a natural compound, morusinol, that specifically destroys the combination of *MSX2* and PU.1, promoting PU.1 degradation and attenuating ovariectomy-induced bone loss. Overall, our results demonstrate that targeting *Msx2* is a promising anabolic therapy for osteoporosis.

Bone is the primary organ that provides support and protection. Disturbed bone homeostasis impairs bone health, leading to osteoporosis and fragility fracture^{1,2}. Bone homeostasis is generally believed to be governed by osteoblast-mediated bone formation and osteoclast-mediated bone resorption². However, in recent years, these views have broadened because multiple cell types, including endothelial cells, neurons, immune cells, and adipocytes, exert various effects on bone cells within the local environment^{3–6}. These findings enrich our understanding of bone metabolism regulation and inspire us to explore novel strategies for osteoporosis treatment.

Post-menopausal osteoporosis (PMOP) is the most common type of osteoporosis. In the bone environment of PMOP, osteoclasts are over-activated and mediate significantly enhanced bone resorption, leading to severe bone loss⁷. Osteoclast is the only cell type in the body capable of absorbing the bone matrix. Induced by macrophage colony-stimulating factor (M-CSF) and receptor activator of nuclear factor- κ B ligand (RANKL), bone marrow monocytes/macrophages (BMMs) could proliferate, fuse, and eventually differentiate into multi-nuclear osteoclasts⁸. Mechanistically, M-CSF and RANKL bind to their receptors CSF1R and RANK, respectively, and stimulate downstream

¹Department of Orthopedic Surgery, Sir Run Run Shaw Hospital, Zhejiang University School of Medicine, Hangzhou, China. ²Key Laboratory of Mechanism Research and Precision Repair of Orthopaedic Trauma and Aging Diseases of Zhejiang Province, Hangzhou, China. ³Department of Orthopedics, Qilu Hospital of Shandong University, Jinan, Shandong, China. ⁴Department of Orthopedics, Xiangya Hospital, Central South University, Changsha, Hunan, China. ⁵Department of Neurology, Sir Run Run Shaw Hospital, School of Medicine, Zhejiang University, Hangzhou, China. ⁶The First Affiliated Hospital of USTC, Division of Life Sciences and Medicine, University of Science and Technology of China, Hefei, China. ⁷Department of Orthopaedics, Shanghai Key Laboratory of Orthopaedic Implant, Shanghai Ninth People's Hospital, Shanghai Jiaotong University School of Medicine, Shanghai, China. ⁸These authors contributed equally: Qingliang Ma, Shiyu Wang, Hong Xue.  e-mail: shunwu_fan@zju.edu.cn; ziang_xie@zju.edu.cn; jiezhwei@zju.edu.cn

signaling pathways such as MAPKs and NF- κ B, leading to the activation of master transcription factors including PU.1 and NFATc1, initiating osteoclastogenesis^{9,10}. Osteoclasts actively participate in bone metabolism and perform endocrine and paracrine functions. Tartrate-resistant acid phosphatase-positive (TRAP⁺) mono-nuclear pre-osteoclasts secrete platelet-derived growth factor-BB (PDGF-BB), which enhances H-type vessel (EMCN^{hi} CD31^{hi}) formation and eventually stimulates osteogenesis¹¹. Therefore, restraining osteoclast fusion and maintaining them in the pre-osteoclast stage could suppress bone resorption while coupling angiogenesis and osteogenesis, exhibiting great potential for osteoporosis treatment.

Characterized by a particular 180 bp homeobox sequence, homeobox genes encode a group of transcription factors containing homeodomain¹². The structure of these genes has been highly conserved during evolution, and they generally play critical roles in embryogenesis, cell proliferation, and differentiation^{13–15}. Multiple homeobox genes have been implicated in the regulation of bone mass and osteogenesis^{16–19}. Nevertheless, the current understanding of the role of homeobox genes in PMOP and osteoclastogenesis remains superficial and scattered, and the hub homeobox genes that regulate PMOP remain unclear. Here, we found that msh homeobox 2 (*MSX2*) plays a central role in PMOP. *MSX2* belongs to the *Msx* family, Antennapedia (ANTP) class of human homeobox genes, and has been reported to be involved in bone development, including skull and tooth formation^{20,21}. Functional haploinsufficiency of *MSX2* causes parietal foramina (PFM), and whole-body *Msx2* knockout mice exhibit pleiotropic defects in bone mass and ectodermal organ formation^{22,23}. Although *Msx2* is generally considered an important regulator of osteogenesis, *Msx2* null mutant mice show an osteopetrosis phenotype in a RANK-dependent manner in skeleton²⁴, suggesting that *Msx2* might also participate in osteoclastogenesis, and its regulatory effect in the bone environment could be complex. However, the direct role of *Msx2* in osteoclast remains unclear.

In this study, we showed that the loss of *Msx2* in myeloid cells leads to increased bone mass. *Msx2* deficiency impairs osteoclast fusion and exerts the role of “brake” in the progression of osteoclast cell fate, which subsequently maintains osteoclasts at the pre-fusion stage. The augmented numbers of pre-osteoclast secrete PDGF-BB, enhancing H-type vessel formation and further coupling osteogenesis. Mechanistically, *MSX2* directly binds to PU.1 and protects it from FBXW7-mediated ubiquitination and degradation. *Msx2* and *Fbxw7* double conditional knockout mice exhibit recovery of bone resorption and osteoclastogenesis. Finally, we screened a natural compound library and found that morusinol, a flavonoid isolated from *Morus alba* root bark, can bind to *MSX2* and release PU.1, promoting PU.1 degradation. The in vivo analysis confirmed the therapeutic effects of morusinol in an ovariectomy (OVX)-induced osteoporosis model. Our results suggest that *MSX2* plays a critical role in PMOP pathogenesis and bone metabolism, coupling osteoclastogenesis with angiogenesis and osteogenesis, and may be a potential target for the treatment of PMOP.

Results

Msx2 is upregulated in post-menopausal osteoporosis and osteoclastogenesis

To identify important homeobox genes in PMOP and osteoclastogenesis, we crossed differentially expressed genes from GSE230665 (RNA-Seq datasets compares PMOP bones with postmenopausal healthy bones, $|\log_{2}FC| > 0.8, p < 0.05$)²⁵ and osteoporosis-related genes from GeneCards database (score > 1) with 298 homeobox genes and found 11 potential target genes (Supplementary Fig. 1a). PPI network analysis suggested that *MSX2* and *IRX3* are hub genes (Supplementary Fig. 1b). According to previous studies, global *Msx2* knockout impairs osteoclast formation, whereas loss of *Irx3* has no effect on osteoclasts^{26,27}. Nevertheless, the direct role of *Msx2* in osteoclastogenesis lacks solid evidence, and the underlying mechanism remains

unclear; therefore, we focused on *Msx2* in this study. To confirm the increased *Msx2* expression level in PMOP, we constructed a mouse OVX model and double-labeled *MSX2* with the osteoclastic marker Cathepsin K (CTSK) on bone sections from the distal femur. As shown in Supplementary Fig. 1c, d, *MSX2*⁺ CTSK⁺ cell number was significantly higher in the OVX group than in the sham group. These results prompted us to explore the expression pattern *Msx2* during osteoclastogenesis. Therefore, we stimulated BMMs with M-CSF and RANKL in vitro and investigated the mRNA and protein levels of *Msx2* during osteoclast formation. The mRNA levels were upregulated on day 3 of osteoclastogenesis and decreased on day 6 (Supplementary Fig. 1e). The protein levels of *Msx2* also peaked on day 3 and remained constant on day 6 (Supplementary Fig. 1f, g). Together, these findings suggest that *Msx2* is upregulated in PMOP and osteoclastogenesis, and may be a potential regulator of osteoclast formation.

Msx2 deficiency in myeloid cells increases bone mass by inhibiting pre-osteoclast fusion

To better understand the role of *Msx2* in bone metabolism and osteoclasts, we generated conditional *Msx2* knockout mice by crossing *Msx2*^{fl/fl} mice with *LysM-Cre* mice (*Msx2* cKO), in which *Msx2* was deficient in myeloid lineage cells. The bone mass of 3-month-old female *Msx2* cKO mice was higher than that of *Msx2*^{fl/fl} controls (Fig. 1a). Micro-computed tomography (Micro-CT) analysis showed that bone volume per tissue volume (BV/TV), trabecular bone number (Tb.N), and cortical bone thickness (Ct.Th) increased, while trabecular bone separation (Tb.Sp) decreased in *Msx2* cKO mice; trabecular bone thickness (Tb.Th) remained unchanged (Fig. 1b). Similar to that in females, *Msx2* deficiency resulted in elevated BV/TV, Tb.N, Ct.Th, and reduced Tb.Sp in males (Supplementary Fig. 2). To precisely describe the changes in bone resorption in *Msx2* cKO mice, we analyzed bone sections of the distal femurs. Although TRAP staining showed comparable numbers of total TRAP-positive cells between *Msx2* cKO mice and controls, the number of multi-nuclear TRAP-positive cells was lower, and that of mononuclear TRAP-positive cells was higher in the *Msx2* cKO group (Fig. 1c, d). Serum CTX-1 levels were also downregulated in *Msx2* cKO mice (Fig. 1e). As more pre-osteoclasts were detected in *Msx2* cKO mice, it was proposed that the fusion stage was impaired by *Msx2* deficiency. Therefore, we performed in vitro osteoclastogenesis assays by inducing BMMs with M-CSF and RANKL. TRAP staining showed that there were comparable numbers of TRAP⁺ cells in *Msx2* cKO and control groups after 3-day stimulation, and these cells were mainly mononuclear. However, cells from *Msx2* cKO mice did not develop mature multi-nuclear TRAP⁺ osteoclasts on day 6, suggesting that the fusion stage of osteoclastogenesis was impaired (Fig. 1f, g). Accordingly, this impairment resulted in the suppression of resorption activity. As shown in Fig. 1h–j, *Msx2* deficient cells generated reduced resorption pit areas on bone slices and produced fewer resorptive enzymes, such as CTSK. To directly compare the fusion ability of cells from *Msx2* cKO and control mice, we performed a double fluorescence labeling assay in which fused cells were defined as double-labeled with both Dil and Hoechst ($N \geq 1$), whereas unfused cells received only a single label (Fig. 1k). Expectedly, *Msx2* deficient cells showed more single labeled cells than control cells when stimulated with RANKL (Fig. 1l). To more accurately evaluate the fusion efficiency of *Msx2* cKO cells, we stained F-actin and nuclei using phalloidin and DAPI, respectively. We calculated normalized number of fusion events as previously reported, equally considering fusions between two mononucleated cells, one mononucleated cell and one multinucleated cell, and two multinucleated cells. As shown in Fig. 1m, n, *Msx2* cKO cells exhibited significantly reduced fusion events. Moreover, we examined genes related to osteoclast fusion and found *Msx2* cKO cells expressed lower levels of *Cd9*, *Cd44*, *Cd47*, *Dcstamp*, and *Ocstamp*, which was consistent with their impaired fusion ability (Fig. 1o). Taken together, these results indicate that *Msx2* deficiency improves bone mass by inhibiting pre-osteoclast fusion.

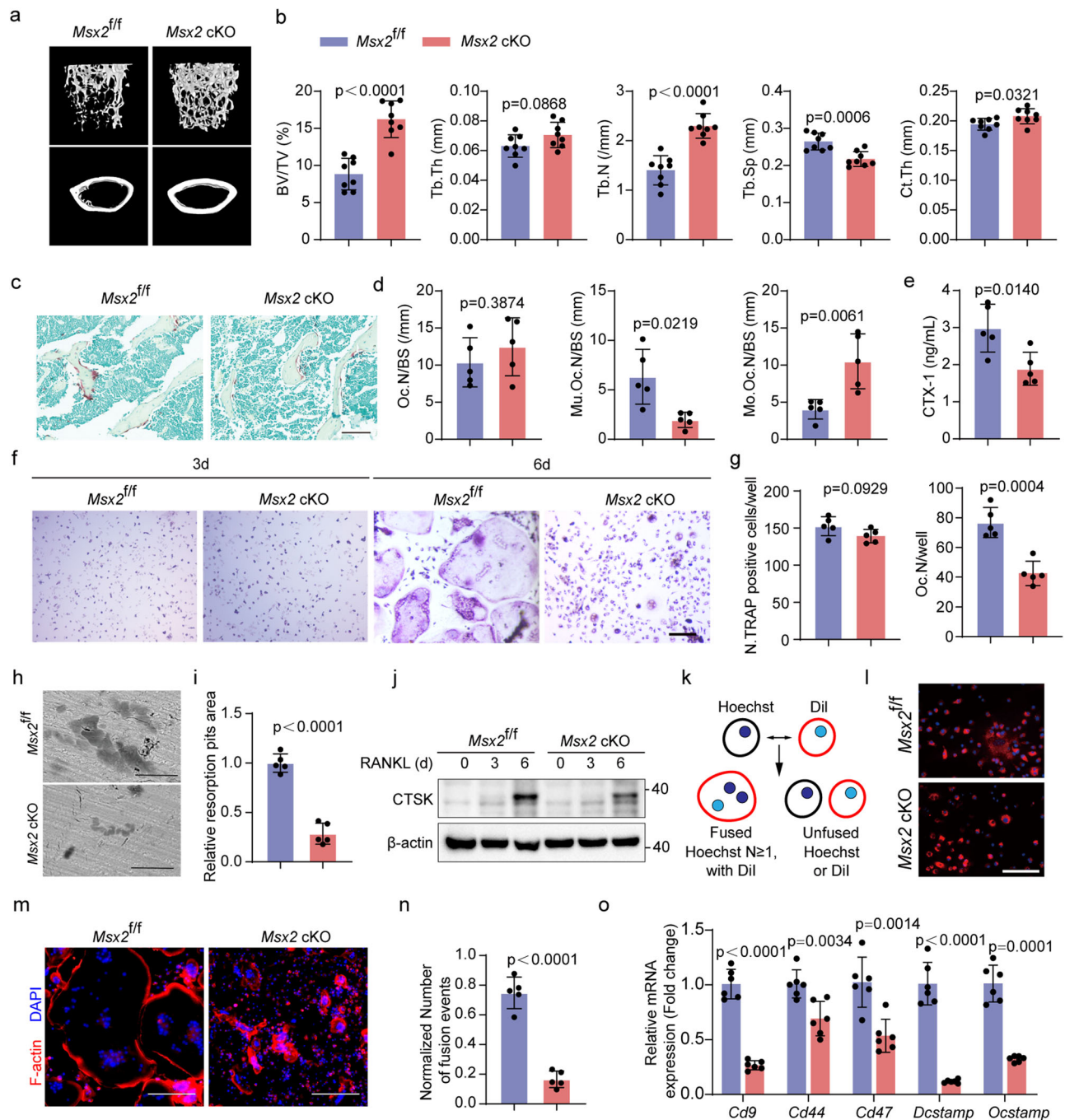


Fig. 1 | Myeloid *Msx2* deficiency improves bone mass through inhibiting pre-osteoclast fusion. **a** Representative 3D Micro-CT images of distal femurs from 3-month-old female *Msx2*^{ff/ff} and *Msx2* cKO mice. **b** Trabecular and cortical bone parameters of *Msx2*^{ff/ff} ($n = 8$) and *Msx2* cKO ($n = 8$) mice. **c** Representative TRAP staining images of distal femurs from 3-month-old female *Msx2*^{ff/ff} and *Msx2* cKO mice. Scale bar, 100 μ m. **d** Histomorphometric analysis of Oc.N/BS, Mu.Oc.N/BS, and Mo.Oc.N/BS ($n = 5$). Mu.Oc.N/BS, multinuclear osteoclast number per bone surface; Mo.Oc.N/BS, mononuclear osteoclast number per bone surface. **e** Serum CTX-1 level ($n = 5$). **f** BMMs were induced by 50 ng/mL RANKL for 3 or 6 days, and representative TRAP staining images were shown. Scale bar, 100 μ m. **g** Quantification of N:TRAP⁺ cells/well and osteoclast number (nuclei) per well (Oc.N/well) ($n = 5$). **h** Representative

SEM images of bone slice resorption pits. Scale bar, 50 μ m. **i** Relative resorption pits area ($n = 5$). **j** BMMs from *Msx2*^{ff/ff} and *Msx2* cKO mice were stimulated by 50 ng/mL RANKL. CTSK protein level were detected during osteoclastogenesis. Representative bands of 3 independent repeats were shown. **k** Schematic showing cell-cell fusion assay. **l** Representative images of cell-cell fusion. Scale bar, 100 μ m. **m** *Msx2*^{ff/ff} and *Msx2* cKO BMMs were stimulated by 50 ng/mL RANKL for 6 days, the cells were stained with phalloidin and DAPI to recognize syncytium. Scale bar, 100 μ m. **n** Quantification of normalized number of fusion events ($n = 5$). **o** Relative mRNA expression level of fusion-related genes of pre-osteoclasts from *Msx2*^{ff/ff} and *Msx2* cKO mice ($n = 6$). Data are presented as mean \pm SD, and p -values were calculated by unpaired, two-tail student's t -test (with Welch's correction when appropriate).

Msx2 deficiency in myeloid cells stimulates osteogenesis and angiogenesis in vivo

The coupling between osteogenesis and H-type vessel formation has been widely reported, and mononuclear pre-osteoclast could secrete PDGF-BB and promote angiogenesis¹¹. Here, *Msx2* deficiency in

osteoclast progenitors also resulted in changes on the bone formation side, with a higher osteocalcin (OCN)-positive cell number, enhanced mineral apposition rate (MAR), and bone formation rate per bone surface (BFR/BS) in *Msx2* cKO mice (Fig. 2a–d). Angiography showed that *Msx2* cKO mice exhibited elevated vessel volume and vessel

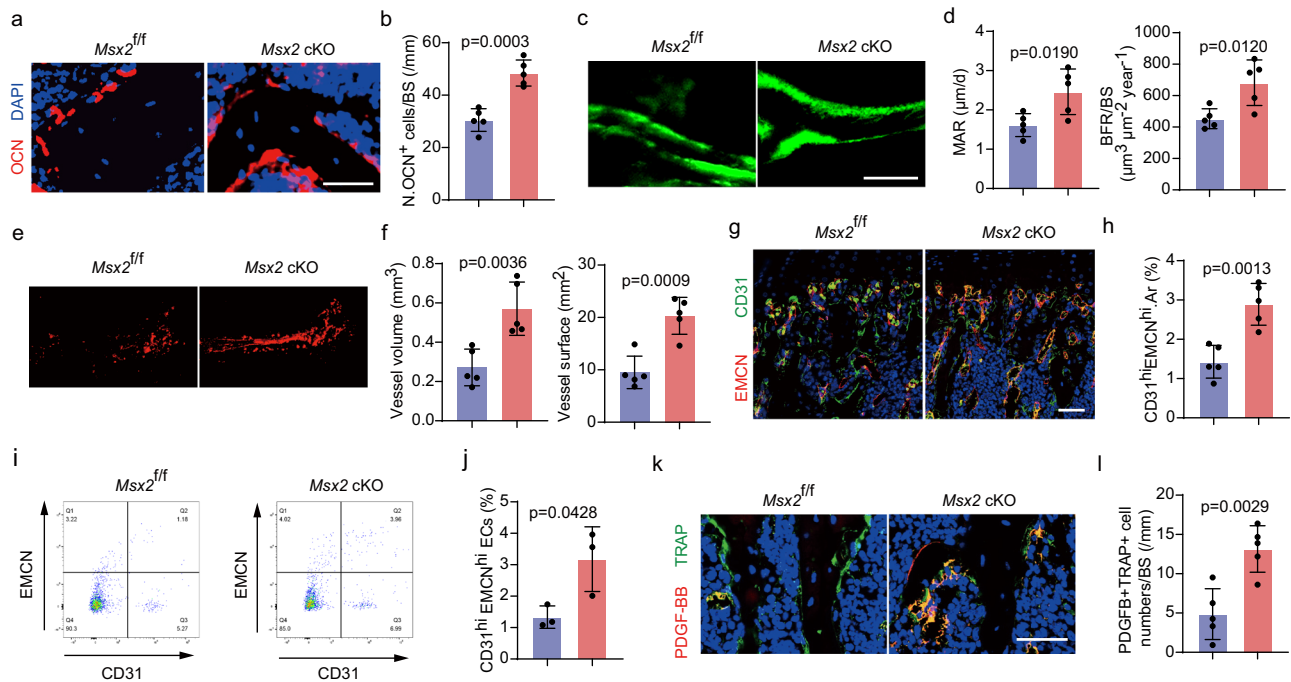


Fig. 2 | Loss of *Msx2* promotes bone formation and angiogenesis. **a** OCN staining of distal femurs from *Msx2*^{fl/fl} and *Msx2* cKO mice. Scale bar, 50 μ m. **b** Quantification of osteocalcin⁺ cell numbers per bone surface (N.OCN⁺ cells/BS) ($n = 5$). **c** Representative images of calcein double labeling of trabecular bones from *Msx2*^{fl/fl} and *Msx2* cKO mice. Scale bar, 25 μ m. **d** Quantification of mineral apposition rate (MAR) and bone formation rate per bone surface (BFR/BS) ($n = 5$). **e** Representative images of femora vessels. **f** Quantification of vessel volume and vessel surface ($n = 5$). **g** EMCN and CD31 immunofluorescence staining of distal femurs from

Msx2^{fl/fl} and *Msx2* cKO mice. Scale bar, 50 μ m. **h** Quantification of CD31^{hi} EMCN^{hi} vessel area in trabecular bones (CD31^{hi} EMCN^{hi}.Ar) ($n = 5$). **i** Representative flow cytometry plots of CD31^{hi} EMCN^{hi} endothelial cells in whole bone marrow cells. **j** Percentage of CD31^{hi} EMCN^{hi} endothelial cells ($n = 3$). **k** Immunofluorescence staining of PDGF-BB and TRAP in distal femurs from *Msx2*^{fl/fl} and *Msx2* cKO mice. Scale bar, 50 μ m. **l** Quantification of PDGF-BB⁺ TRAP⁺ cell numbers per bone surface ($n = 5$). Data are presented as mean \pm SD, and p -values were calculated by unpaired, two-tail student's t -test.

surface in the bones (Fig. 2e, f). The number of H-type vessels (CD31^{hi} EMCN^{hi}) was also increased (Fig. 2g, h). Flow cytometry further supported our finding that more CD31^{hi} EMCN^{hi} endothelial cells were detected in the bone marrow of *Msx2* cKO mice (Fig. 2i, j). PDGF-BB⁺ TRAP⁺ cells are considered to be the main population of pre-osteoclasts that induce angiogenesis¹¹. Therefore, we performed immunofluorescence staining and found more PDGF-BB⁺ TRAP⁺ cells in *Msx2* cKO mice (Fig. 2k, l). Collectively, the loss of *Msx2* in myeloid cells increases bone mass by impairing osteoclastogenesis and enhancing angiogenesis and osteogenesis in vivo.

***Msx2* deficiency promotes vessel formation of endothelial cells in vitro**

To further confirm the effect of *Msx2* deficiency on vessel formation, we first detected differences in PDGF-BB secretion between samples derived from *Msx2* cKO and control pre-osteoclasts. *Msx2* cKO cells exhibited higher *Pdgfb* expression levels and produced more PDGF-BB in the medium (Supplementary Fig. 3a–c). Subsequently, we cultured human umbilical vein endothelial cells (HUVECs) with conditioned media derived from *Msx2* cKO and control pre-osteoclasts (Supplementary Fig. 3d). The wound-healing assay showed that HUVECs cultured in *Msx2* cKO medium exhibited elevated migration activity (Supplementary Fig. 3e, f). The Matrigel tube formation assay also indicated that *Msx2* cKO conditioned medium enhanced HUVECs tube formation (Supplementary Fig. 3g, h). The osteogenic ability of bone marrow mesenchymal stem cells (BMSCs) was not affected by myeloid *Msx2* conditional knockout (Supplementary Fig. 3i). Moreover, no significant changes in osteogenesis were observed when wild-type BMSCs were treated with conditioned media from *Msx2* cKO and control pre-osteoclasts in vitro (Supplementary Fig. 3j). These results suggest that myeloid *Msx2* deficiency enhances vessel formation of

endothelial cells and that the observed promoting effect on osteogenesis in vivo is indirect.

MSX2 promotes pre-osteoclast fusion through stabilizing PU.1

Given the increased mRNA levels of fusion-related genes such as *Cd9*, *Cd44*, *Cd47*, *Dcstamp*, and *Ocstamp*, we used the Signaling Pathways Project data of Genecards database to identify their common transcription factors (TFs). This analysis revealed 18 TFs (Supplementary Fig. 4a). Notably, MSX2 is not among these 18, although it is a well-known TF. Another important role of MSX2 is to serve as a co-transcriptional regulator and to affect mRNA expression through other TFs. Therefore, we analyzed the CHIP-Seq data of fusion-related genes from Genecards, and PU.1 (Spi1) showed a relatively higher frequency and binding score in all five fusion-related genes, which means PU.1 is the most probable TF regulating fusion-related genes (Supplementary Fig. 4b–f). Thus, MSX2 likely regulates the expression of fusion-related genes via PU.1. Overexpressing of PU.1 indeed rescued the formation of multinucleated osteoclasts and the expression of fusion-related genes (Fig. 3a–c). To further explore the effect of MSX2 on PU.1, we investigated whether *Msx2* knockout altered the expression of PU.1. After treating *Msx2*^{fl/fl} BMMs with Cre or *Msx2* adenoviruses, the protein level of PU.1 was altered, whereas the mRNA level of PU.1 remained unchanged (Fig. 3d–f). Moreover, knocking out *Msx2* enhanced PU.1 degradation when treated with cycloheximide (CHX) (Fig. 3g, h), whereas overexpression of MSX2 suppressed PU.1 degradation (Supplementary Fig. 5a, b). To clarify the PU.1 degradation pathway, we used the proteasome inhibitor MG132 or the lysosome inhibitor chloroquine (CQ) to treat *Msx2*^{fl/fl} and *Msx2* cKO pre-osteoclasts, respectively. Protein degradation of PU.1 was prevented by MG132 treatment, while CQ showed no rescue effect, suggesting that MSX2 regulated PU.1 protein degradation mainly through the

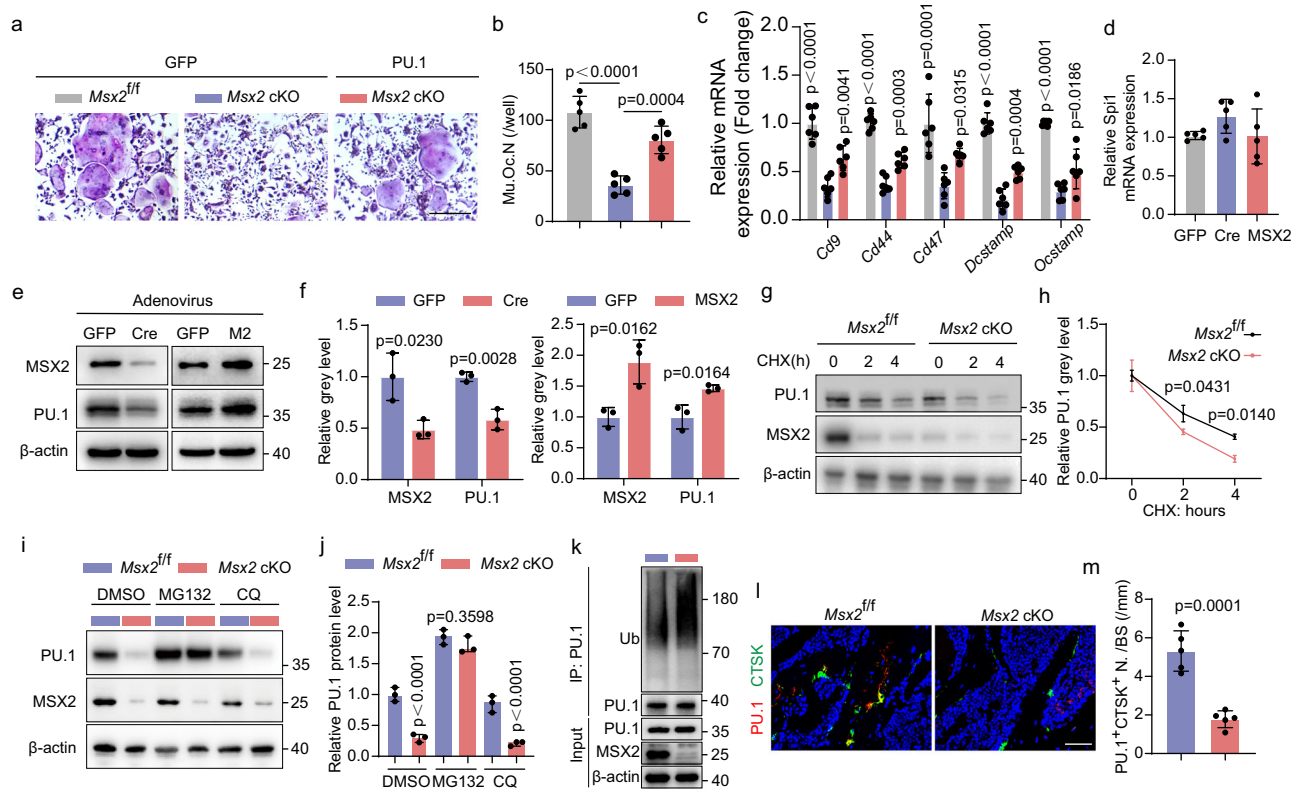


Fig. 3 | *Msx2* promotes pre-osteoclast fusion through stabilizing PU.1. **a** BMMs were infected by GFP or PU.1 adenovirus and then stimulated by RANKL. Representative images of TRAP staining were shown. Scale bar, 100 μ m. **b** Quantification of Oc.N/well in **(a)** ($n = 5$). **c** BMMs were infected by GFP or PU.1 adenovirus and then stimulated by RANKL for 3 days. Relative mRNA expressions of fusion related genes were measured ($n = 5$). **d** BMMs were infected by GFP, Cre, or MSX2 adenovirus and then stimulated by RANKL, relative PU.1 mRNA expression was measured ($n = 5$). **e** BMMs were treated as stated in **(d)**, and representative images of MSX2 and PU.1 protein bands were shown. **f** Quantification of MSX2 and PU.1 relative grey levels ($n = 3$). **g** BMMs from *Msx2*^{fl/fl} and *Msx2* cKO mice were induced by RANKL for 3 days, then cells were treated by cycloheximide (CHX) for indicated hours, the protein levels of PU.1 and MSX2 were detected. **h** Quantification of PU.1 relative grey level.

i BMMs from *Msx2*^{fl/fl} and *Msx2* cKO mice were induced by RANKL for 3 days, then cells were treated by DMSO, MG132, or chloroquine (CQ) for 4 h, the protein levels of PU.1 and MSX2 were detected. **j** Relative PU.1 protein level was measured ($n = 3$). **k** BMMs from *Msx2*^{fl/fl} and *Msx2* cKO mice were induced by RANKL for 3 days. Cells were treated with MG132 for 4 h, and Co-IP was performed to examine the ubiquitination level of PU.1. **l** PU.1 and CTSK immunofluorescence staining of distal femurs from *Msx2*^{fl/fl} and *Msx2* cKO mice. Scale bar, 100 μ m. **m** Quantification of PU.1⁺ CTSK⁺ cell numbers per bone surface (PU.1⁺ CTSK⁺ N./BS) ($n = 5$). Data are presented as mean \pm SD, and p -values were calculated by unpaired, two-tail student's t -test (**f** and **m**), one-way ANOVA with Tukey's multiple comparisons (**b–d**) and two-way ANOVA with Sidak's multiple comparisons (**h** and **j**).

proteasome pathway (Fig. 3i, j). Subsequently, we performed ubiquitination assays and found *Msx2* cKO pre-osteoclasts exhibited increased PU.1 ubiquitination (Fig. 3k). In contrast, overexpression of MSX2 attenuated PU.1 ubiquitination, similar results were obtained in the 293T cell line (Supplementary Fig. 5c, d). To further confirm the reduced PU.1 level in osteoclast in vivo, we labeled PU.1 with osteoclastic marker, CTSK, in bone sections and found the number of PU.1⁺ CTSK⁺ cells was significantly reduced in *Msx2* cKO mice (Fig. 3l, m). Because PU.1 is crucial for myeloid differentiation, we examined the expression of F4/80, a marker of mature monocytes and macrophages, in bone sections from *Msx2* cKO mice. The expression level of F4/80 was comparable in *Msx2*^{fl/fl} and *Msx2* cKO mice, indicating that myeloid *Msx2* deficiency does not influence on myeloid differentiation and osteoclast precursor formation (Supplementary Fig. 5e, f). In summary, MSX2 promotes the expression of osteoclast fusion-related genes by preventing the proteasome-mediated degradation of PU.1 without affecting macrophage and osteoclast precursor development.

MSX2 binds PU.1 and protects it from FBXW7-mediated ubiquitination

To further explore how MSX2 protects PU.1, we hypothesized that MSX2 directly binds to PU.1. Immunofluorescence labeling revealed that MSX2 and PU.1 are both nuclear (Fig. 4a). The Co-IP assay further confirmed the direct combination of MSX2 and PU.1 in both BMMs and

HEK-293T cells (Fig. 4b, c). To investigate whether this combination affected PU.1 degradation, we searched for the potential E3 ubiquitin ligases related to PU.1 using UbiBrowser and found FBXW7²⁸. FBXW7 is the only E3 ubiquitination ligase for PU.1 that has been confirmed by literature in UbiBrowser database (Fig. 4d). Expectedly, exogenous MSX2 significantly reduced the ubiquitination level of PU.1, which was rescued by FBXW7 overexpression in HEK-293T cells (Fig. 4e). Intriguingly, the MSX2 binding region in PU.1 was also the critical motif responsible for FBXW7 recognition. Specifically, we analyzed the amino acid sequence of PU.1 and found three loci in accordance with the FBXW7 phosphodegron motifs (S/TxxxS/T), which was consistent with a previous study²⁹ (Fig. 4f). Molecular docking assays revealed that MSX2 sheltered PU.1-Ser41 and Ser142, blocking their recognition by FBXW7 (Fig. 4g). We further mutated PU.1-Ser41 and PU.1-Ser142 (PU.1-MUT: PU.1-S41A, S142A) and found that FBXW7 could promote PU.1 ubiquitination, however, this effect was canceled by PU.1 mutation (Fig. 4h). Overall, MSX2 served as a protector by concealing PU.1-Ser41 and Ser142, thereby preventing PU.1 from being ubiquitinated by FBXW7 (Fig. 4i).

Msx2 Fbxw7 double knockout blunts the bone phenotype of *Msx2* cKO mice

FBXW7 has been reported to participate in osteoclastogenesis and mice with osteoclast-specific *Fbxw7* ablation (*Fbxw7*^{fl/fl} *Ctsk*-Cre) exhibit

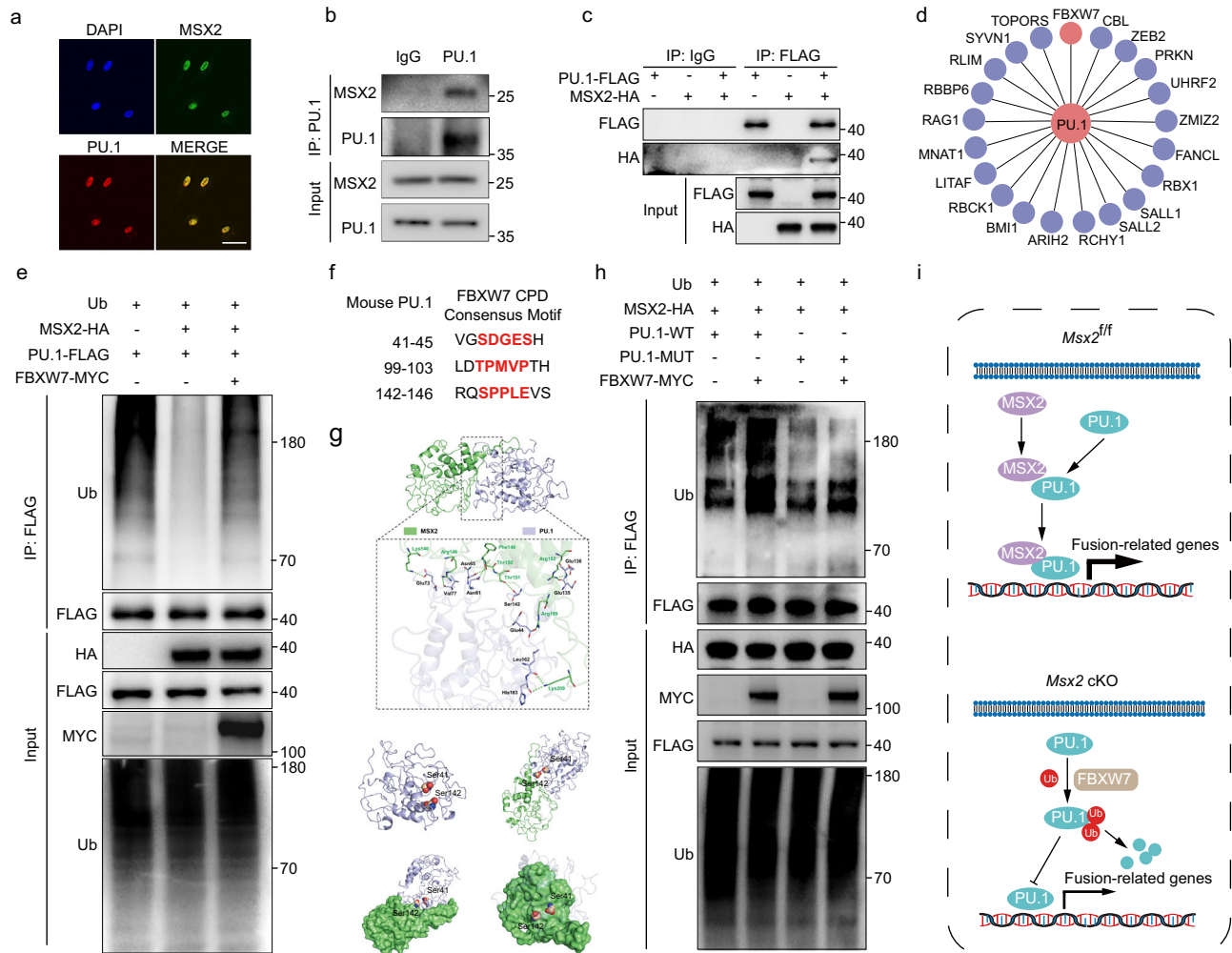


Fig. 4 | MSX2 binds PU.1 and protects it from FBXW7 mediated ubiquitination.

a BMMs were stimulated by RANKL for 3 days, and immunofluorescence staining of MSX2 and PU.1 in BMMs were captured. Scale bar, 20 μ m. **b** BMMs were stimulated by RANKL for 3 days, and Co-IP was performed to show the interaction between MSX2 and PU.1. **c** HEK-293T cells were transfected by PU.1-FLAG and MSX2-HA, and the interaction between MSX2 and PU.1 were examined. **d** Prediction of the E3 ubiquitination ligase of PU.1 using Ubiquitizer. **e** HEK-293T cells were transfected

as indicated and then treated by MG132 for 6 h. The ubiquitination level of PU.1 was detected by Co-IP. **f** The FBXW7 CPD consensus motif in mouse PU.1. **g** Molecular docking of MSX2 and PU.1 complex. **h** HEK-293T cells were transfected as indicated and then treated by MG132 for 6 h. The PU.1 ubiquitination levels were detected by Co-IP. **i** Schematic of the protective effect of MSX2 on PU.1 ubiquitination degradation. All experiments were repeated 3 times independently, and the representative images were shown (**a–c**, **e**, and **h**).

osteoporotic phenotype³⁰. Here, we found that myeloid *Fbxw7* deficiency (*Fbxw7^{fl/fl} LysM-Cre, Fbxw7* cKO) also led to low bone mass, with reduced BV/TV, Tb.Th, Tb.N, and elevated Tb.Sp (Supplementary Fig. 6a, b). Loss of *Fbxw7* promotes osteoclastogenesis both in vivo and in vitro (Supplementary Fig. 6c–f). Consistently, PU.1 protein level was upregulated by *Fbxw7* knockout (Supplementary Fig. 6g). To better confirm the relationship between MSX2, PU.1, and FBXW7 in vivo, we bred *Msx2^{fl/fl} Fbxw7^{fl/fl} LysM-Cre* mice (dKO), in which both *Msx2* and *Fbxw7* were knocked out in myeloid cells. As expected, PU.1 protein levels were restored by the double knockout (Supplementary Fig. 7a). The Co-IP assay revealed a lower ubiquitination level of PU.1 by double knockout (Supplementary Fig. 7b). The in vitro osteoclastogenesis assay showed recovery of multi-nuclear TRAP-positive cell numbers (Supplementary Fig. 7c, d). The bone slice resorption assay indicated that the double knockout rescued the bone resorptive pit area (Supplementary Fig. 7e, f). Additionally, the normalized number of cell fusion events was partially recovered by the double knockout (Supplementary Fig. 7g, h). Subsequently, we analyzed the bone phenotypes in vivo. The bone mass of dKO mice was lower than that of *Msx2* cKO mice, and bone parameters were altered correspondingly (Fig. 5a–c). Furthermore, bone section staining showed that the

number of multi-nuclear TRAP-positive cells was recovered in dKO mice, whereas OCN-positive cells were decreased (Fig. 5d–g). The number of H-type vessels also decreased (Fig. 5h, i). Furthermore, while the number of PDGF-BB and TRAP double-positive cells was increased in *Msx2* cKO mice, the double knockout significantly reduced this population (Fig. 5j, k). In conclusion, using an *Msx2 Fbxw7* double knockout mouse model, we further confirmed that MSX2 protects PU.1 from FBXW7-mediated ubiquitination.

Targeting MSX2 by morusinol prevents bone loss in OVX mice

Given that *Msx2* deficiency led to elevated bone mass, we hypothesized that targeting MSX2 could be a potential therapy for osteoporosis. To test this hypothesis, we investigated the bone phenotypes of *Msx2^{fl/fl}* and *Msx2* cKO mice after ovariectomy. As shown in Supplementary Fig. 8a, b, OVX surgery led to a reduction of BV/TV from $8.497 \pm 1.412\%$ to $2.508 \pm 1.012\%$ (approximately 70.5% loss) in *Msx2^{fl/fl}* mice, while the proportion of bone loss in *Msx2* cKO mice was 60.3% (from $14.54 \pm 1.861\%$ to $5.712 \pm 1.224\%$). Moreover, *Msx2* cKO mice exhibited increased Tb.N, Ct.Th, and decreased Tb.Sp after OVX (Supplementary Fig. 8b). Histological analysis revealed that *Msx2* deficiency resulted in fewer multi-nuclear osteoclasts, and

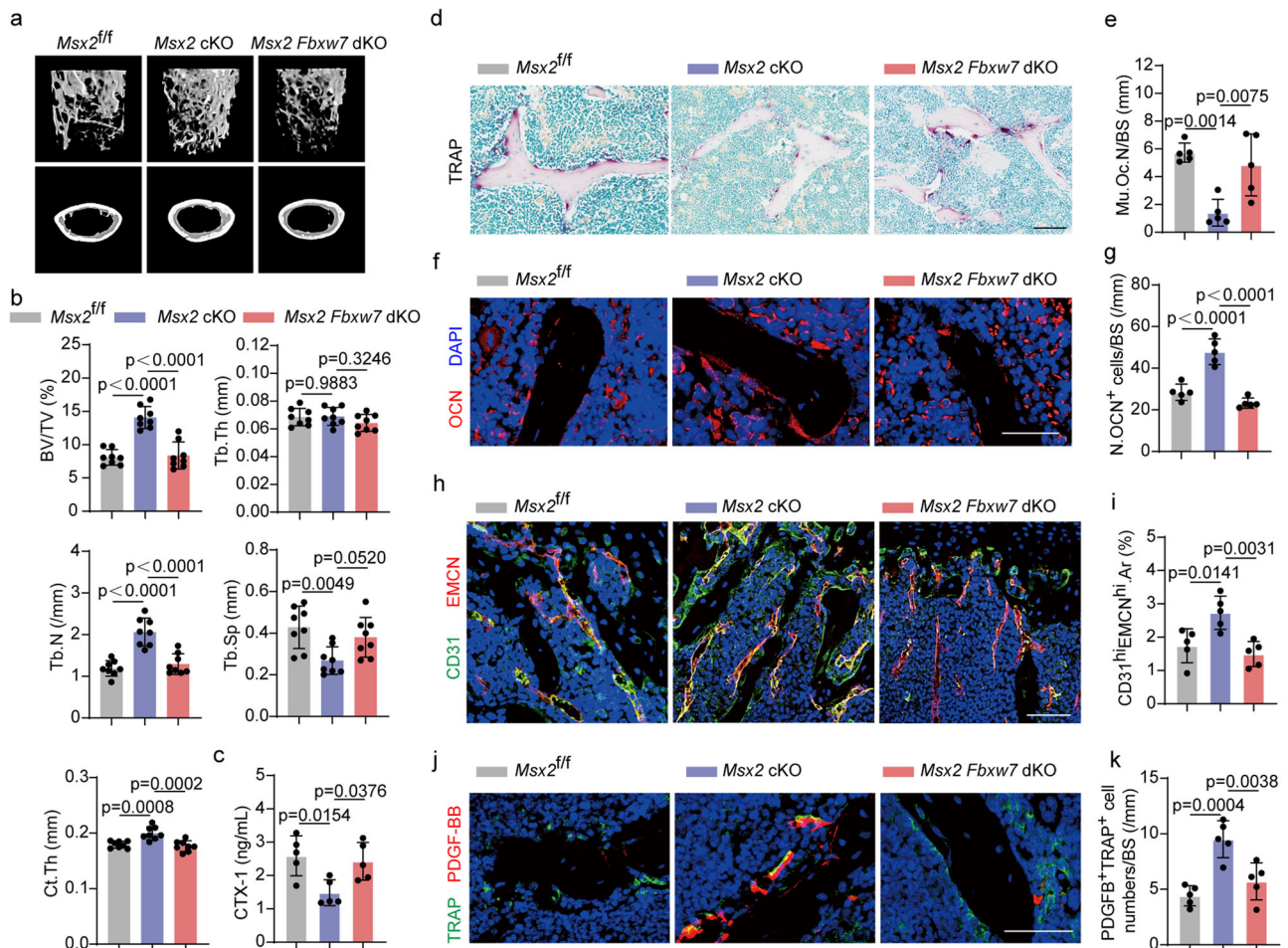


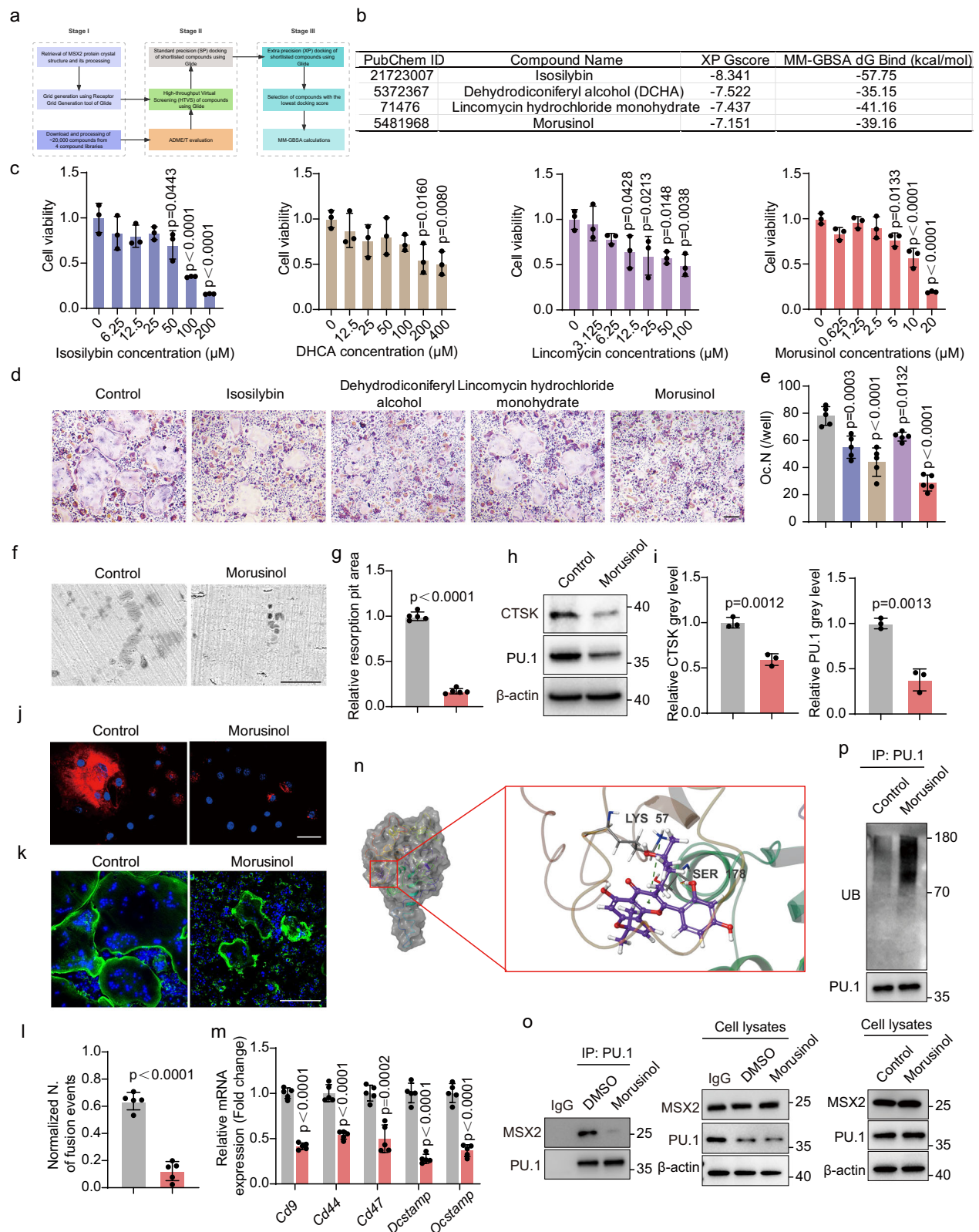
Fig. 5 | *Msx2 Fbxw7* double knockout blunts the bone protective effect of *Msx2* deficiency. **a** Representative 3D Micro-CT images of distal femurs from 3-month-old female *Msx2^{fl/fl}* and *Msx2* cKO and *Msx2 Fbxw7* dKO mice. **b** Bone morphology parameters of distal femurs from *Msx2^{fl/fl}* ($n=8$), *Msx2* cKO ($n=8$), and *Msx2 Fbxw7* dKO ($n=8$) mice. **c** Serum CTX-1 level of *Msx2^{fl/fl}*, *Msx2* cKO, and *Msx2 Fbxw7* dKO mice ($n=5$). **d** Representative TRAP staining images of distal femurs from *Msx2^{fl/fl}*, *Msx2* cKO, and *Msx2 Fbxw7* dKO mice. Scale bar, 100 μ m. **e** Quantification of

Mu.Oc.N/BS in **(d)** ($n=5$). **f** OCN immunofluorescence staining of distal femurs. Scale bar, 50 μ m. **g** N.OCN⁺ cells/BS was measured ($n=5$). **h** Representative images of EMCN and CD31 immunofluorescence staining of distal femurs. Scale bar, 50 μ m. **i** CD31^{hi} EMCN^{hi} Ar was measured ($n=5$). **j** Representative images of PDGF-BB and TRAP immunofluorescence staining. Scale bar, 50 μ m. **k** Quantification of PDGF-BB⁺ TRAP⁺ cell numbers/BS ($n=5$). Data are presented as mean \pm SD, and p -values were calculated using one-way ANOVA with Tukey's multiple comparisons.

serum CTX-1 levels were also reduced (Supplementary Fig. 8c–e). On the bone formation side, *Msx2* cKO mice showed more OCN-positive cells, higher MAR and BFR/BS (Supplementary Fig. 8f–i). Consistently, angiogenesis was more active in *Msx2* cKO mice, with more EMCN^{hi} CD31^{hi} vessels (Supplementary Fig. 8j, k). These results confirmed that the bone protective effects of *Msx2* deficiency also exist in the OVX mouse model.

Natural compounds have shown advantages in terms of safety, effectiveness, and convenience in disease treatment³¹; therefore, we screened approximately 20,000 natural compounds using high-throughput virtual screening (HTVS) to identify potential compounds that could interrupt the MSX2-PU.1 combination. According to the XP Gscore and molecular mechanics-generalized born surface area (MM-GBSA) dG Bind, we identified 13 molecules that showed a relatively high affinity for MSX2, of which four molecules could form direct interactions with MSX2, including isosilybin, dehydronicoferyl alcohol, lincomycin hydrochloride monohydrate, and morusinol (Fig. 6a, b). After determining the concentrations used for in vitro treatment, we incubated BMMs with these drugs under RANKL stimulation (Fig. 6c). TRAP staining revealed that morusinol exerted the strongest suppressive effect on osteoclastogenesis (Fig. 6d, e). A bone resorption assay confirmed the inhibitory effect of morusinol on

osteoclast function (Fig. 6f, g). The protein level of CTSK and PU.1 was also reduced by morusinol (Fig. 6h, i). To evaluate whether morusinol affects osteoclast fusion, we performed fusion assay in which the morusinol group exhibited significant decreased number of Hoechst⁺ Dil1⁺ cells (Fig. 6j). Via F-actin staining, we found that morusinol reduced the number of osteoclast fusion events (Fig. 6k, l). Consistently, osteoclast fusion-related gene expression was also suppressed by morusinol (Fig. 6m). To determine whether these effects of morusinol were exerted through MSX2 and PU.1, we performed molecular docking between morusinol and MSX2, which showed that morusinol forms hydrophobic interactions with Val³² and Leu¹⁷⁹, a hydrogen bond interaction with Ser¹⁷⁸, and π -cation with Lys³³ (Fig. 6n). These amino acid residues are important for the interaction between MSX2 and PU.1; thus, morusinol may inhibit osteoclastogenesis by interrupting the combination of MSX2 and PU.1 and promoting PU.1 degradation. As expected, the Co-IP assay indicated that the MSX2-PU.1 complex was reduced under morusinol treatment, while ubiquitinated PU.1 was upregulated (Fig. 6o, p). To further confirm whether morusinol works through the MSX2-FBXW7 axis, we employed morusinol in *Fbxw7* cKO cells and found that *Fbxw7* deficiency could rescue morusinol-mediated osteoclast inhibition (Supplementary Fig. 9a, b). Accordingly, the expression of fusion-related genes and the protein level of



PU.1 and CTSC were recovered (Supplementary Fig. 9c, d). Since natural products generally exhibit extensive polypharmacology, and morusinol reportedly regulates beta3-integrin, tumor necrosis factor, and interleukin 1 beta involved in osteoclastogenesis, we profiled expression changes of these potential targets under morusinol treatment^{34–36}. As shown in Supplementary Fig. 9e, morusinol subtly influenced the expression of representative pro-inflammatory

cytokines, including *Il-1b*, *Tnf-a*, and *Il-6*, only slightly enhancing *Il1-b*. Although morusinol significantly reduced beta3-integrin (Supplementary Fig. 9f), it may also be a downstream effect of PU.1, which has been reported to transactivate beta3-integrin in concert with NFATc1³⁷. Although we cannot completely exclude the polypharmacology of morusinol, our results indeed prove that MSX2-FBXW7 axis is important for the actions of morusinol.

Fig. 6 | Morusinol targets MSX2-PU.1 complex and inhibits osteoclast fusion. **a** Strategy of high throughput virtual screening. **b** Information of the most likely MSX2-targeting natural compounds. **c** BMMs were incubated with indicated concentrations of drugs for 48 h, the cell viability was detected by CCK-8 assay and normalized to control group ($n = 3$). **d** BMMs were stimulated by RANKL accompanied with isosilybin (25 μM), DCHA (100 μM), lincomycin hydrochloride monohydrate (6.25 μM), or morusinol (2.5 μM), respectively. Representative images of TRAP staining were shown. Scale bar, 100 μm . **e** Quantification of Oc.N/well in (**d**) ($n = 5$). **f** Bone resorption assay of morusinol treatment. Scale bar, 50 μm . **g** Quantification of relative resorption pits area ($n = 5$). **h** Protein level of PU.1 and CTSK under morusinol treatment. **i** Relative PU.1 and CTSK grey level in (**h**) ($n = 3$). **j** Cell-cell fusion under morusinol treatment. Scale bar, 100 μm . **k** BMMs were

stimulated by 50 ng/mL RANKL and 2.5 μM morusinol for 6 days, the cells were stained with phalloidin and DAPI. Scale bar, 100 μm . **l** Quantification of normalized number of fusion events ($n = 5$). **m** Relative mRNA expression of osteoclast fusion-related genes ($n = 5$). **n** Three-dimensional image of molecular docking between morusinol and MSX2. **o** Protein level of PU.1 and CTSK under morusinol treatment. **p** BMMs were stimulated by RANKL with or without morusinol for 3 days, then cells were treated by MG132 for 4 h. Co-IP assay was performed to detect the combination of MSX2 and PU.1. **q** BMMs were stimulated by RANKL with or without morusinol for 3 days, then cells were treated by MG132 for 4 h, the ubiquitination level of PU.1 was examined. Data are presented as mean \pm SD, and p -value were calculated by unpaired, two-tail student's t test (**g**, **i**, **l**, and **m**) or one-way ANOVA with Dunnett's multiple comparisons (**c** and **e**).

The positive in vitro results prompted us to further investigate the potential therapeutic effects of morusinol in an OVX mouse model. As shown in Fig. 7a, mice were injected daily with 30 mg/kg morusinol for 6 weeks after sham surgery or ovariectomy. Micro-CT results confirmed the beneficial effects of morusinol on bone mass, manifested by rescued BV/TV, Tb.Th, Ct.Th, and reduced Tb.Sp (Fig. 7b, c). Regarding bone resorption, TRAP staining showed that OVX mice exhibited increased multi-nuclear osteoclasts and reduced mono-nuclear osteoclasts, whereas morusinol treatment reversed this trend (Fig. 7d, e). Morusinol also reduced serum CTX-1 concentration in OVX mice (Fig. 7f). Moreover, we double-labeled PU.1 and CTSK in OVX and OVX + morusinol groups. The number of PU.1⁺ CTSK⁺ cells was significantly reduced by morusinol in OVX models, indicating morusinol promotes PU.1 degradation in osteoclasts in vivo (Fig. 7g, h). Similar to that in *Msx2* cKO mice, morusinol treatment did not affect macrophage development (Supplementary Fig. 10). In terms of bone formation, morusinol treatment increased OCN-positive cells and enhanced MAR and BFS/BS (Fig. 7i–l). Regarding angiogenesis, EMCN^{hi} CD31^{hi} vessels were reduced in the OVX group, whereas morusinol treatment rescued vessel formation (Fig. 7m, n). Overall, targeting MSX2 with morusinol inhibits bone resorption, enhances bone and vessel formation, and protects bone mass.

Discussion

In this study, we identified *Msx2* as a critical homeobox gene that modulates bone homeostasis. *Msx2* expression is upregulated in PMOP bones and during osteoclastogenesis. As shown in Fig. 8, knocking out *Msx2* increases bone mass by attenuating osteoclastogenesis and enhancing angiogenesis-mediated bone formation. At the cellular level, *Msx2* deficiency inhibits cell fusion and results in a larger population of pre-osteoclasts, leading to the enhanced secretion of PDGF-BB. High levels of PDGF-BB promote H-type vessel formation and subsequently stimulate osteogenesis. Molecularly, MSX2 prevents PU.1, one of the master transcription factors involved in osteoclast formation, from FBXW7-mediated ubiquitination and degradation. MSX2 binding sheltered the key motif of PU.1 from FBXW7 recognition. These findings prompted us to screen natural compounds targeting MSX2 and identify morusinol, which directly disrupts the MSX2-PU.1 complex and serves as an anabolic therapy for osteoporosis.

Homeobox genes are a large and diverse group of genes characterized by possessing at least one 180 bp homeobox DNA sequence that encodes a highly conserved 60 amino acid homeodomain¹². Homeodomain proteins are generally considered transcription factors or co-transcription factors that play vital roles in diverse physiological and pathological processes³⁸. Approximately 15% of all transcription factors within the animal genome are homeodomain proteins. Studies have shown that homeodomain protein families, such as *MSX*, *DLX*, and *PBX*, regulate cranium and limb development during embryogenesis^{39–41}. Moreover, it has been reported that homeodomain proteins play an active role in adult bone mass regulation^{42,43}. Nevertheless, most existing studies have focused on the impact of homeodomain proteins on osteogenesis, with little understanding of

their roles in osteoclastogenesis. A few studies have revealed that homeobox genes, such as *Lhx2*, *Dlx5*, and *Pax6*, affect osteoclast formation^{44–46}; however, these minority studies are fragmented and unsystematic. Here, we used the expression profiles of PMOP bones to identify 11 osteoporosis-related homeobox genes. PPI network analysis indicated *MSX2* as a hub gene. Furthermore, in vitro and in vivo experiments confirmed elevated *Msx2* expression in osteoporotic bones and osteoclastogenesis. Collectively, these results inspired us to explore the potential role of MSX2 in osteoclast formation and bone resorption.

Voluminous previous studies have reported that MSX2 is closely associated with bone development. *MSX2* mutations cause Boston-type craniosynostosis, and haploinsufficiency of human *MSX2* causes deficient ossification around the parietal notch²³. In mouse models, whole-body *Msx2* deficient mice are viable but with a variety of malformations, including PFM, defective cerebellum, tooth, hair follicle, and mammary gland development²². *Msx2* deficient P30 mice exhibit an osteopenia phenotype with predominant osteoblast defects. These phenotypes are considered to be associated with the crucial role of *Msx2* in osteoblast differentiation. It has been reported that *Msx2* promotes primary murine osteoblast differentiation and calcification in concert with typical osteoblastic transcription factors, and ectopic *Msx2* rescues the impaired osteoblastogenesis induced by *Runx2* deficiency^{47,48}. Mechanistically, *Msx2* expression responds to BMP2/4, and further activates canonical Wnt signaling in osteoblast progenitors^{49,50}. Notably, there are also studies suggesting the potentially important role of *Msx2* in osteoclastogenesis. In a *Msx2*^{-/-} transgenic mouse model, *Msx2* null mutation leads to periodontal osteopetrosis, with impaired osteoclast generation in alveolar bones²⁶. It has also been reported that *Msx2* deficient adult mice show a slight osteopetrosis phenotype in the skull, tibia, and mandible, which could be reversed by RANK overexpression²⁴. Therefore, the role of *Msx2* in different types of bone cells is complex, and conditional *Msx2* deficient models are warranted. In this study, we found that PMOP bone samples showed increased *Msx2* expression in osteoclasts, indicating that *Msx2* in osteoclasts also plays an important role in bone metabolism during adulthood. We generated myeloid-specific *Msx2* deficiency mice and demonstrated that knocking out *Msx2* in osteoclast progenitors improves bone mass, with impaired osteoclastogenesis mainly manifesting as impaired osteoclast fusion rather than reduced osteoclast numbers. Although our results confirmed the direct role of MSX2 in osteoclasts and bone homeostasis, osteoblast-specific *Msx2* knockout and inducible gene knockout systems are still needed to characterize the effect of MSX2 on bone mass more precisely.

In recent years, an increasing number of studies have demonstrated that bones exhibit important endocrine and paracrine behaviors. Crosstalk between different cells in the bone environment provides new insights into the regulation of bone metabolism and general health. The most classic and well-known interaction between bone cells is that osteoblast lineage cells could secrete RANKL and induce osteoclastogenesis⁵¹. In 2014, Xie et al. first reported that pre-fusion osteoclasts release PDGF-BB, which promotes H-type vessel

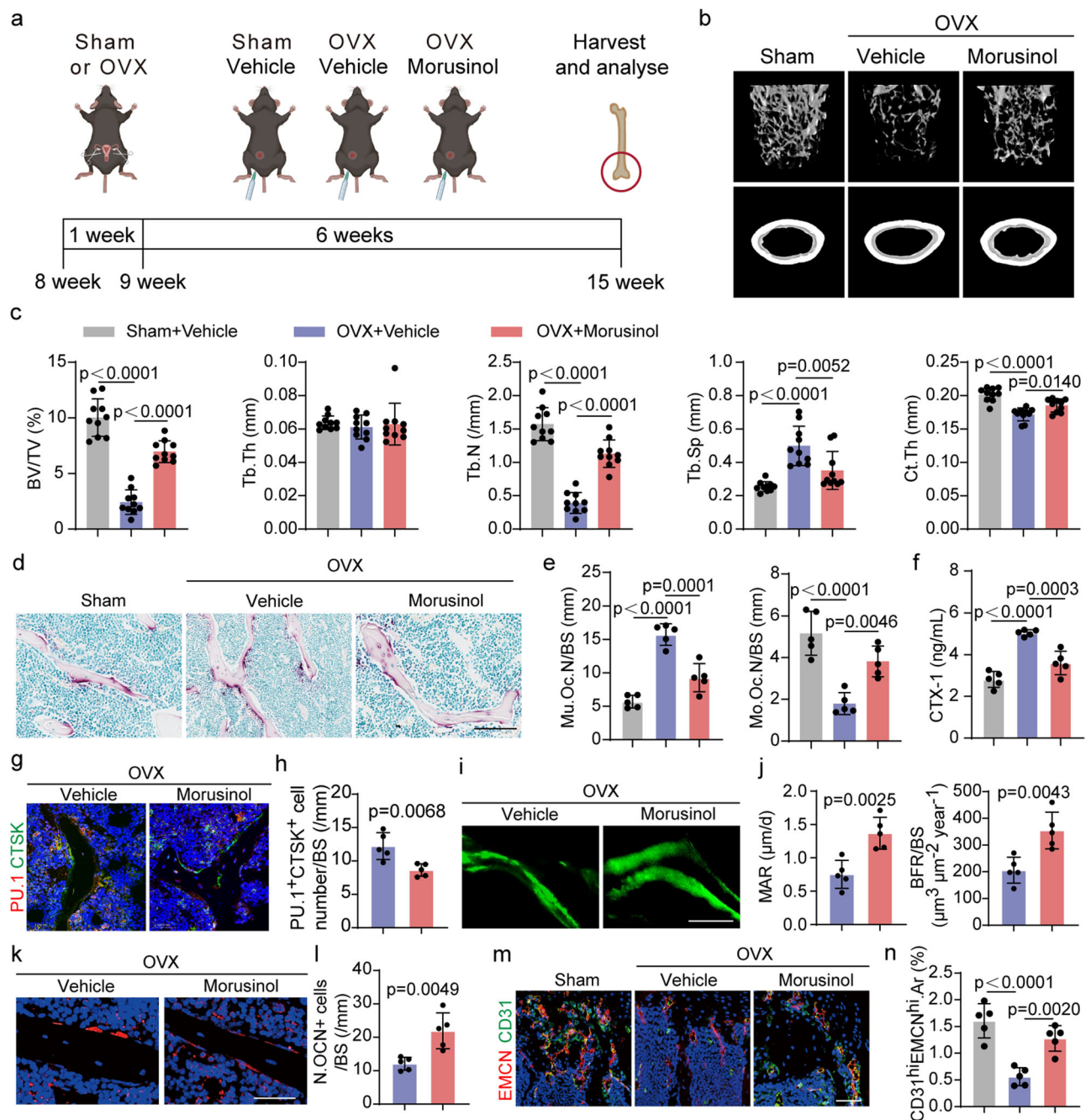


Fig. 7 | Targeting MSX2 by morusinol prevents bone loss in OVX mice.

a Schematic diagram for morusinol treatment in OVX mice, created by Biorender. **b** The 3D Micro-CT images of distal femurs from mice in Sham, OVX, and OVX + morusinol groups. **c** Bone morphology parameters of distal femurs ($n=10$). **d** Representative TRAP staining images from Sham, OVX, and OVX + morusinol groups. Scale bar, 100 μm . **e** Quantification of Mu.Oc.N/BS and Mo.Oc.N/BS ($n=5$). **f** Serum CTX-1 levels were detected by ELISA ($n=5$). **g** Immunofluorescence staining of PU.1 and CTSK in distal femurs from OVX and OVX + morusinol groups. Scale bar, 50 μm . **h** Quantification of PU.1⁺ CTSK⁺ cell number/BS ($n=5$). **i** Calcein

labeling images from OVX and OVX + morusinol groups. Scale bar, 25 μm .

j Quantification of MAR and BFR/BS ($n=5$). **k** Immunofluorescence staining of OCN in distal femurs from OVX and OVX + morusinol groups. Scale bar, 50 μm . **l** OCN⁺ cells/BS was measured ($n=5$). **m** Representative images of immunofluorescence staining of EMCN^{hi} CD31^{hi} vessels. Scale bar, 50 μm . **n** Quantification of CD31^{hi} EMCN^{hi}.Ar ($n=5$). Data are presented as mean \pm SD, and p -values were calculated by unpaired, two-tail student's t -test (**h**, **j**, and **l**) and one-way ANOVA with Tukey's multiple comparisons (**c**, **e**, **f**, and **n**).

formation and subsequently stimulates osteogenesis⁵¹. Since then, molecules affecting osteoclast fusion and angiogenesis, such as SIGLEC15, L-plastin, and TLR2, have been successively discovered^{52–54}. Antibodies targeting these molecules have also been developed⁵². Moreover, a recent study also demonstrated that adipocytes in bone marrow could couple angiogenesis through estrogen-related receptor α ⁵⁵. These studies emphasize the important role of angiogenesis in mediating bone cell crosstalk and regulating bone mass. Here, we

demonstrate that *Msx2* deficiency in myeloid cells reduces bone resorption and increases bone mass. Additionally, we observed that angiogenesis-mediated bone formation was enhanced as a secondary effect of osteoclast-specific *Msx2* knockout. These findings are attributed to the role of MSX2 in osteoclast fusion. Specifically, *Msx2* deficiency impairs osteoclast fusion and exerts the role of “brake” in the progression of osteoclast cell fate, leading to increased pre-osteoclast numbers and PDGF-BB secretion.

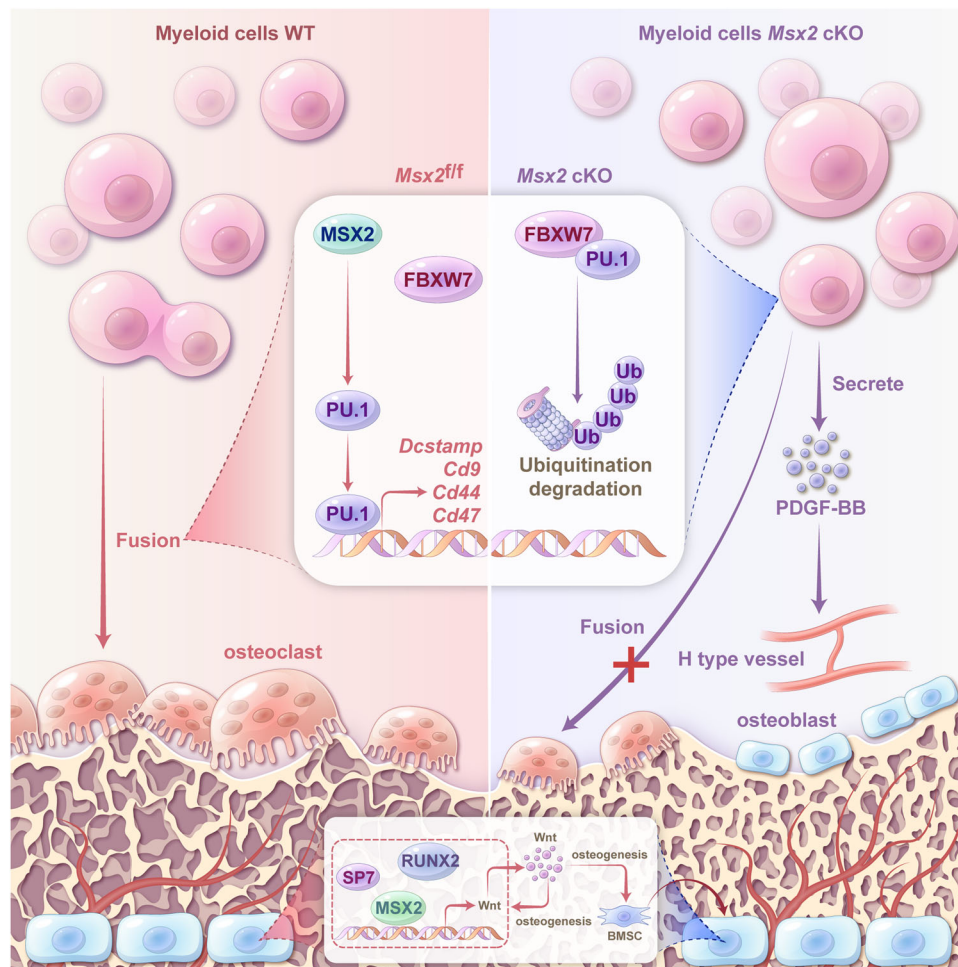


Fig. 8 | Schematic diagram of targeting *Msx2* as a brake in the fusion fate of osteoclast and an anabolic therapy for osteoporosis. In wild-type myeloid cells, MSX2 binds PU.1 and prevents PU.1 from FBXW7 mediated ubiquitination, which safeguards fusion cell fate of osteoclast and results in bone resorption. Targeting *Msx2* promotes PU.1 degradation and acts as a “brake” in the progression of the fusion fate of osteoclast, resulting in a larger population of pre-osteoclasts. Pre-

osteoclasts secrete PDGF-BB and enhance angiogenesis-mediated bone formation (upper part of Fig. 8). Since voluminous prior studies have reported that MSX2 is important in regulating Wnt signaling and bone formation in concert with osteogenic transcription factors, myeloid-specific targeting MSX2 is necessary to achieve net anabolic effects (lower part of Fig. 8). The schematic diagram was designed by Figdraw.

Osteoclast fusion is a well-organized process triggered by RANKL, during which mono-nuclear pre-osteoclasts form multi-nuclear mature osteoclasts. The fusion process involves proteins that mediate recognition and initial association between fusing cells, fusogens that drive the actual fusion events, and various accessory proteins⁵⁶. Classic fusion-related proteins in osteoclastogenesis include CD9, CD44, CD47, OC-STAMP, and DC-STAMP, the most well-known fusogen⁵⁶. In recent years, novel fusion-related proteins such as SIGLEC15, L-plastin, and TLR2 have been identified^{52–54}. In this study, we showed that the expression of classic fusion-related molecules in osteoclastogenesis is downregulated in *Msx2* cKO mice. However, PU.1, rather than MSX2, was predicted to be the common transcription factor of fusion-related genes. Considering PU.1 participates in the entire process of osteoclast differentiation and promotes osteoclast commitment and maturity of osteoclast^{33,57,58}, we proposed that the “brake” role of targeting MSX2 acts on PU.1-“clutch”. Indeed, we found that MSX2 could regulate PU.1 protein levels without affecting PU.1 mRNA levels. Mechanistically, MSX2 could directly bind to PU.1 and prevent it from FBXW7-mediated degradation. FBXW7 is known to recognize a conserved S/TxxxS/T motif^{59,60}, and we found that the key phosphorylation loci of PU.1 (Ser41, Ser142) are sheltered by MSX2, leading to reduced ubiquitination and degradation of PU.1. *Msx2* and *Fbxw7* double knockout rescued PU.1, and subsequently osteoclast fusion, which was also

confirmed *in vivo*. These results demonstrate that MSX2 could prevent PU.1 from FBXW7-mediated degradation through direct binding. Nevertheless, although our results provide sufficient evidence for the indirect role of MSX2 in fusion-related genes through PU.1, it is still difficult to rule out the direct transcriptional effect of MSX2 on these genes.

Anti-resorptive drugs such as bisphosphonates and denosumab are the first-line agents for osteoporosis treatment. However, these drugs cause severe adverse events, poor compliance, and easy recurrence⁶¹, which prompt us to identify and develop new drugs. Recently, drugs such as teriparatide and romosozumab have been developed and applied clinically, drawing more attention to anabolic therapeutic strategies for osteoporosis treatment⁶². In this study, we demonstrated that targeting MSX2 could be an anabolic strategy. Knocking out *Msx2* in osteoclast progenitors inhibited bone resorption, enhanced angiogenesis-mediated bone formation, and rescued bone mass in an OVX-induced osteoporosis mouse model. In addition, the expression pattern of *Msx2* indicates that targeting MSX2 primarily affects the osteoclast fusion stage, which evades the potential risk of PU.1 deficiency in myeloid development. Natural products are critical sources of drugs. Compared to synthetic compounds and biological agents, natural products have greater molecular rigidity, which makes them more valuable in tackling protein-protein interactions.

Moreover, their use in traditional medicine provides helpful references for efficiency and safety³¹. In this study, we found that morusinol can target MSX2 and disrupt the interaction between MSX2 and PU.1. Morusinol treatment attenuates multi-nuclear osteoclast formation both in vitro and in vivo. Meanwhile, morusinol promoted vessel formation and osteogenesis. Although we could not completely exclude the polypharmacology of morusinol, our results indicated that morusinol exhibits great potential for the treatment of osteoporosis.

In conclusion, this study demonstrates that *Msx2* is a critical homeobox gene regulating osteoclastogenesis and bone homeostasis. Targeting MSX2 acts as a “brake” in the progression of osteoclast cell fate by promoting PU.1 degradation, which subsequently enhances angiogenesis-mediated bone formation. Morusinol targets MSX2 and serves as an anabolic therapy for osteoporosis.

Methods

Mice

The *LysM-Cre* (#004781) mice and *Msx2*^{fl/fl} mice (#025441) were from Jackson Laboratory (USA). Mice carrying *Fbxw7* conditional null alleles (*Fbxw7*^{fl/fl}, NM-CKO-200327) were from Shanghai Model Organisms (Shanghai, China). *Msx2*^{fl/fl} mice were crossed with *LysM-Cre* mice to generate *Msx2*^{fl/+}, *LysM-Cre*⁺ mice. Myeloid-specific *Msx2* deletion was obtained by breeding *Msx2*^{fl/+}, *LysM-Cre*⁺ mice with *Msx2*^{fl/fl} mice, and *Msx2*^{fl/fl} littermates were used as control. Three-month-old female and male mice samples were collected for further analysis. Myeloid-specific *Fbxw7* deletion was acquired by crossing *Fbxw7*^{fl/fl} mice with *LysM-Cre* mice through a similar strategy. Three-month-old female *Fbxw7*^{fl/fl}, *LysM-Cre*⁺ mice and their littermate controls were used for phenotype assessment. To obtain *Msx2*, *Fbxw7* dKO mice, *Msx2*^{fl/fl}, *LysM-Cre*⁺ mice were firstly crossed with *Fbxw7*^{fl/fl} mice to generate *Msx2*^{fl/+}, *Fbxw7*^{fl/+}, *LysM-Cre*⁺ mice, which were then crossed with *Msx2*^{fl/fl} mice to obtain *Msx2*^{fl/fl}, *Fbxw7*^{fl/+}, *LysM-Cre*⁺ mice. The *Msx2*^{fl/fl}, *LysM-Cre*⁺ mice and *Msx2*^{fl/fl}, *Fbxw7*^{fl/fl}, *LysM-Cre*⁺ mice were generated by breeding *Msx2*^{fl/fl}, *Fbxw7*^{fl/+}, *LysM-Cre*⁺ mice with *Msx2*^{fl/fl}, *Fbxw7*^{fl/+} mice, and the *Msx2*^{fl/fl} littermates were used as control. Three-month-old female *Msx2*, *Fbxw7* dKO mice were used for further evaluation. Female wild-type C57BL/6 mice were purchased from SLAC Laboratory Animal Company (Shanghai, China). All animal procedures were ethically approved by Sir Run Run Shaw Hospital Committee for Animal Resources, and were conducted in compliance with the approved ethical guidelines. Mice were housed under a 12 h dark/12 h light cycle, 22 °C ambient temperature, and 50% humidity. All mice were routinely genotyped using standard PCR protocols, and the primers used are listed in Supplementary Table 1. All experimental animals in this study were anesthetized by intraperitoneal injection of 1% sodium pentobarbital before surgery or sacrifice to reduce the pain.

Ovariectomy (OVX)-induced osteoporosis mouse model

Eight-week-old female mice were anesthetized and subjected to a sham operation or bilateral ovariectomy. All mice were given 1 week for postoperative recovery. *Msx2*^{fl/fl} and *Msx2* cKO mice were euthanized 6 weeks after recovery. Femur and blood samples were collected for further analysis. For the morusinol treatment, 30 mice were randomly categorized into three groups: Sham, OVX, and OVX + morusinol, with 10 mice per group. Morusinol was dissolved in dimethyl sulfoxide and diluted in PBS (vehicle). Mice from the Sham and OVX groups received vehicle injections daily, whereas mice in the OVX + morusinol group received morusinol injections (30 mg/kg/day) one week after the surgery. After a 6-week injection period, the mice were sacrificed for further analysis.

Micro-CT

The femurs were scanned using a Skyscan 1275 instrument (Bruker). The scanning parameters were set as follows: 50 kV, 200 mA, and 9 μm voxel size. For the region of interest (ROI), we selected sections from

100 slices below the growth plate to 300 slices below the growth plate for trabecular bones, and from 300 slices below the growth plate to 350 slices below the growth plate for cortical bones. Bone parameters, including BV/TV, Tb.Th, Tb.N, Tb.Sp, and Ct.Th, were analyzed using CTAn software (Bruker). The 3D reconstructed images were obtained by stacking the 2D images from the ROI using the CTVox software (Bruker).

Bone histology and immunofluorescence

The femurs were fixed with 4% paraformaldehyde for 48 h and then decalcified for 2 weeks. The samples were then embedded in paraffin and cut into 4-μm-thick sections. TRAP staining was performed using a commercial kit (Sigma-Aldrich). For the immunofluorescence staining, we incubated bone sections with primary antibodies at 4 °C overnight. The antibodies used for immunofluorescence analysis were OCN (ab93876, Abcam), CTSK (sc-48353, Santa Cruz), MSX2 (DF4126, Affinity), CD31 (ab182981, Abcam), EMCN (sc-65495, Santa Cruz), PDGF-BB (ab23914, Abcam), and TRAP (ab191406, Abcam). The sections were then incubated with fluorescence-conjugated secondary antibodies for 2 h at room temperature. The images were captured using a fluorescence microscope, and we quantified the positively stained cells in five randomly selected fields of the distal metaphysis of femurs using Halo software.

Angiography

Bone blood vessel imaging was conducted using Micro-CT according to previous reports^{63,64}. Mice were anesthetized, the left ventricle was exposed, and a needle was inserted. The vasculature was washed with saline solution 3 times and then fixed with 4% paraformaldehyde. The vessel dye (MV-120, Flow Tech) was then injected into the vasculature. Subsequently, mice were incubated at 4 °C overnight to crosslink the dye, and then femurs were collected and decalcified for 2 weeks. The decalcified bones were subjected to micro-CT scanning, and the vessel volume and vessel surface were measured.

Flow cytometry

Flow cytometry was performed as previously reported⁵³. Briefly, fresh femurs from *Msx2*^{fl/fl} and *Msx2* cKO mice were collected, and the muscles, periosteum, and epiphysis were removed. The bone marrow was flushed and collected, and the bones were crushed in cold PBS and digested by collagenase together with the flushed bone marrow at 37 °C for 20 min to obtain the whole bone marrow cells. After filtration and washing, the cells were then incubated with an APC-conjugated CD31 antibody (17-0311-82, eBioscience), PE-conjugated EMCN monoclonal antibody (sc-65495, Santa Cruz), BV510 conjugated TER119 antibody (563995, BD Horizon), or FITC-conjugated CD45 antibody (553079, BD Pharmingen). Fluorescence-activated cell sorting (FACS) was performed, and CD31⁺CD45⁺TER119⁻ cells were sorted as bone marrow endothelial cells.

Calcein double labeling

Calcein (#C7600) was purchased from Solarbio (Beijing, China). Calcein double labeling experiments were conducted as previously described³². Briefly, mice were intraperitoneally injected with calcein (15 mg/kg) 10 and 3 days before euthanasia. Femurs were collected and sectioned. Calcein labels were captured using a fluorescence microscope, and the MAR was calculated according to a previously reported standard⁶⁵.

In vitro osteoclastogenesis

The femurs and tibias of 6-week-old mice were collected and used for BMMs extraction. Bone marrow cells were flushed out and cultured in complete α-MEM supplemented by 30 ng/mL M-CSF (416-ML, R&D) for 4 days. Non-adherent cells were removed, and BMMs were seeded into 96-well plates at a density of 8000 cells/well. For osteoclast

stimulation, cells were induced with 30 ng/mL M-CSF and 50 ng/mL RANKL (462-TEC, R&D) for 5–6 days until multi-nuclear osteoclasts were generated.

Preparation of conditional medium

Conditioned medium derived from pre-osteoclast was prepared according to previous reports^{11,53}. Briefly, BMMs were stimulated with 30 ng/mL M-CSF and 50 ng/mL RANKL for 3 days to generate pre-osteoclasts. The serum-containing pre-osteoclast-derived conditional medium was collected 2 days after pre-osteoclast formation. To obtain serum-free conditional medium, the cells were then cultured for 1 more day in a serum-free medium supplemented with M-CSF and RANKL, and the medium was collected. All conditional media were centrifuged (1000 × g, 10 min, 4 °C) and stored at –80 °C before use. Serum-containing conditioned medium was used for the tube formation and osteogenesis assays, while serum-free conditioned medium was used for the wound healing assay.

Bone slice resorption assay

The bone resorption assay was conducted as previously reported⁶⁶. Briefly, BMMs were seeded onto bovine bone slices at a density of 8000 per well and stimulated with 50 ng/mL RANKL. After mature osteoclasts were generated, the cells were treated with RANKL for 5 days. Then, bone slices were collected, and cells were gently removed from the surface of the bone slices. Resorption pits were observed using a scanning electron microscope.

Cell-cell fusion assay

The cell-cell fusion assay was performed as described previously⁶⁷. Briefly, BMMs were incubated with 30 ng/mL M-CSF and 50 ng/mL RANKL for 3 days. The cells were collected and categorized into two equal duplicates. Each duplicate cells were labeled with either Hoechst (40731ES, Yeason, 5 µg/mL, 37 °C, 5 min) or CM-Dil (40718ES, Yeason, 2.5 µM, 37 °C, 15 min). The labeled cells were washed 3 times with PBS, and then equal cells with a single label (Hoechst or CM-Dil) were cultured together under 30 ng/mL M-CSF and 100 ng/mL RANKL. Fluorescence images were captured 12 h later.

Fusion efficiency calculation

To precisely evaluate the fusion efficiency of osteoclasts, we calculated the normalized number of fusion events according to a previous report. Osteoclasts were fixed with 4% paraformaldehyde for 15 min and then permeabilized by Triton-100 for 5 min. The F-actin of syncytia was stained by phalloidin (CA1610, Solarbio) for 1 h at room temperature, and the nuclei were stained by DAPI (C0060, Solarbio). The fluorescence images were captured using Nikon fluorescence microscopy. The normalized number of fusion events was calculated as $\Sigma(N_i - 1)/N_{\text{total}}$, in which N_i equals the number of nuclei in a syncytium, and N_{total} equals the total number of nuclei in syncytia and unfused cells. $N_i - 1$ could precisely reflect the number of fusion events to form a syncytium with N_i nuclei irrespective of whether the syncytium was generated by fusion between two mono-nuclear cells, one mono-nuclear cell and one multi-nuclear cell or two multi-nuclear cells; N_{total} was used to normalize the subtle discrepancy of cell density among samples.

In vitro osteogenesis

BMSCs were isolated as previously reported⁵⁵. For in vitro osteogenesis, BMSCs were incubated with a mixed medium: 50% osteogenic medium (10% FBS, 50 µg/mL ascorbic acid, 5 mM β-glycerophosphate, and 100 mM dexamethasone in α-MEM) and 50% serum-containing conditional medium from pre-osteoclast. ALP staining was performed 7 days after stimulation, and ARS staining was performed 21 days after stimulation.

In vitro tube formation

In vitro tube formation assays were performed using Matrigel (356237; BD Biosciences) and prepared according to the manufacturer's instructions. HUVECs (CL-0675, Procell) were incubated with a mixed medium: 50% endothelial cell medium and 50% conditioned media derived from *Msx2*^{fl/fl} and *Msx2* cKO pre-osteoclasts for 12 h. The Matrigel was polymerized in 24-well plates at 37 °C and the cells were seeded on the gel at a density of 150,000 per well. After incubation at 37 °C for another 4 h, the tube formation pictures were captured using a microscope.

Wound healing assay

HUVECs were seeded into a 6-well plate and cultured until they reached confluence. Cells were wounded using a sterile pipette tip and imaged under a microscope. The cells were then treated with serum-free conditional media derived from *Msx2*^{fl/fl} and *Msx2* cKO pre-osteoclasts. Twelve hours later, the wounds were captured again, and the migration area was calculated according to a previous report⁶⁸.

RNA extraction and real-time PCR

Total RNA was extracted with an Ultrapure RNA extraction kit purchased from CWBio. RNA was reverse-transcribed using a reverse transcription kit (Accurate Biotechnology). Real-time PCR was performed using 2 × SYBR Green Pro Taq HS Premix (Accurate Biotechnology) according to the manufacturer's instructions. The relative gene expressions were calculated with the –ΔCT method, and β-actin was used as the internal control. The primers used in this study are listed in Supplementary Table 2.

Plasmid transfection and adenovirus infection

The plasmids used in this study were commercially constructed using the pcDNA3.1 vector by GeneChem, and all the tags were fused on the C terminus. For plasmid transfection, HEK-293T cells (CL-0005, Procell) were transfected with 2 µg plasmid using lipofectamine 3000 and P3000 for 24 h. The medium was then changed, and the cells were cultured for another 48 h before the experiments.

Cre, MSX2, and PU.1 adenovirus were commercially constructed using pAdM-FH-GFP vector by WZBiosciences. For adenovirus infection, BMMs were cultured and infected with adenovirus (MOI = 50) for 6 h, then the media were changed, and BMMs were cultured for another 48 h before the experiments.

Immunoblots

The cells were lysed in RIPA lysis buffer containing protease inhibitors. The extracted proteins were then subjected to immunoblot assays, as previously reported³². The primary antibodies used in this study were anti-NFATc1 (sc-7294, Santa Cruz), anti-MSX2 (ab227720, Abcam), anti-β-actin (66009-1-Ig, Proteintech), anti-CTSK (sc-48353, Santa Cruz), anti-PU.1 (ab227835, Abcam), anti-FLAG (20543-1-AP, Proteintech), anti-HA (51064-2-AP, Proteintech), anti-MYC (16286-1-AP, Proteintech), anti-Ubiquitin (10201-2-AP, Proteintech), and anti-FBXW7 (28424-1-AP, Proteintech). After overnight incubation with primary antibodies at 4 °C, corresponding HRP-conjugated secondary antibodies were used for band detection.

Co-IP

The Co-IP assay was performed as previously reported³². Briefly, cell lysates were immunoprecipitated with anti-PU.1 or anti-FLAG overnight at 4 °C. The mixture was then incubated with protein A/G agarose beads (36417ES; Yeason). Next, the immune complexes were collected and subjected to immunoblotting. Primary antibodies from different sources and specific secondary antibody (AS062, Abclonal and abs20213, Absin) were used to avoid heavy/light chain interference.

Molecular docking and HTVS

The structures of MSX2 and PU.1 were constructed using Alphafold and optimized using PROCHECK^{69,70}. Molecular docking was performed using HDOCK, according to previous reports^{71,72}. For HTVS, we selected the interaction site of MSX2 as a docking pocket and performed HTVS. Standard precision and extra precision (XP) analyses were performed to identify the top hits. The MM-GBSA was calculated to quantitatively determine the binding affinity between the small molecules identified by XP and MSX2. The threshold values were set as follows: XP GScore ≤ 7 , MM-GBSA dG Bind < -30 kcal/mol.

Statistical analyses

All data are presented as means \pm SD. Differences were determined using GraphPad Prism software (version 8.0). Unpaired two-tailed student's *t*-test was used for two-group comparisons. One-way and two-way ANOVAs with post-hoc tests for comparisons of more than two groups are shown in the figure legends. Differences were considered significant at $p < 0.05$.

Reporting summary

Further information on research design is available in the Nature Portfolio Reporting Summary linked to this article.

Data availability

Source data are provided with this paper. Genes expression profiles of PMOP in femur were previously published in [GSE230665](https://doi.org/10.1038/s41467-025-61938-0). All supporting data are available for reproducibility purposes from the corresponding author upon request. Source data are provided with this paper.

References

- Compston, J. E., McClung, M. R. & Leslie, W. D. Osteoporosis. *Lancet* **393**, 364–376 (2019).
- Weivoda, M. M. & Bradley, E. W. Macrophages and bone remodeling. *J. Bone Miner. Res.* **38**, 359–369 (2023).
- Liu, X., Zhang, P., Gu, Y., Guo, Q. & Liu, Y. Type H vessels: functions in bone development and diseases. *Front. Cell Dev. Biol.* **11**, 1–10 (2023).
- Chen, Y., Guo, B., Ma, G. & Cao, H. Sensory nerve regulation of bone homeostasis: emerging therapeutic opportunities for bone-related diseases. *Ageing Res. Rev.* **99**, 102372 (2024).
- Fischer, V. & Haffner-Luntzer, M. Interaction between bone and immune cells: implications for postmenopausal osteoporosis. *Semin. Cell Dev. Biol.* **123**, 14–21 (2022).
- Li, J., Chen, X., Lu, L. & Yu, X. The relationship between bone marrow adipose tissue and bone metabolism in postmenopausal osteoporosis. *Cytokine Growth Factor Rev.* **52**, 88–98 (2020).
- Song, S., Guo, Y., Yang, Y. & Fu, D. Advances in pathogenesis and therapeutic strategies for osteoporosis. *Pharm. Ther.* **237**, 108168 (2022).
- Elson, A., Anuj, A., Barnea-Zohar, M. & Reuven, N. The origins and formation of bone-resorbing osteoclasts. *Bone* **164**, 116538 (2022).
- Jiang, T., et al. Role and regulation of transcription factors in osteoclastogenesis. *Int. J. Mol. Sci.* **24**, 16175 (2023).
- Takayanagi, H. RANKL as the master regulator of osteoclast differentiation. *J. Bone Min. Metab.* **39**, 13–18 (2021).
- Xie, H., et al. PDGF-BB secreted by preosteoclasts induces angiogenesis during coupling with osteogenesis. *Nat. Med.* **20**, 1270–1278 (2014).
- García-Fernández, J. The genesis and evolution of homeobox gene clusters. *Nat. Rev. Genet.* **6**, 881–892 (2005).
- Zhao, J. et al. PDX1 + cell budding morphogenesis in a stem cell-derived islet spheroid system. *Nat. Commun.* **1**, 18 (2024).
- Kim, K. H., Rosen, A., Bruneau, B. G., Hui, C. C. & Backx, P. H. Iroquois homeodomain transcription factors in heart development and function. *Circ. Res.* **110**, 1513–1524 (2012).
- Kuriki, M., Korb, A., Comai, G. & Tajbakhsh, S. Interplay between Pitx2 and Pax7 temporally governs specification of extraocular muscle stem cells. *PLoS Genet.* **20**, 1–27 (2024).
- Yu, X. et al. TGF β -induced factor homeobox 2 blocks osteoblastic differentiation through targeting pSmad3/HDAC4/H4ac/Runx2 axis. *J. Cell Physiol.* **234**, 21284–21293 (2019).
- Yang, H., Liang, Y., Cao, Y., Cao, Y. & Fan, Z. Homeobox C8 inhibited the osteo-/dentinogenic differentiation and migration ability of stem cells of the apical papilla via activating KDM1A. *J. Cell Physiol.* **235**, 8432–8445 (2020).
- Heo, J. S., Lee, S. G. & Kim, H. O. Distal-less homeobox 5 is a master regulator of the osteogenesis of human mesenchymal stem cells. *Int. J. Mol. Med.* **40**, 1486–1494 (2017).
- Xu, J. et al. Shox2 regulates osteogenic differentiation and pattern formation during hard palate development in mice. *J. Biol. Chem.* **294**, 18294–18305 (2019).
- Babajko, S., de La Dure-Molla, M., Jedeon, K. & Berdal, A. MSX2 in ameloblast cell fate and activity. *Front. Physiol.* **6**, 1–10 (2015).
- Alappat, S., Zhang, Z. Y. & Chen, Y. P. Msx homeobox gene family and craniofacial development. *Cell Res.* **13**, 429–442 (2003).
- Satokata, I. et al. Msx2 deficiency in mice causes pleiotropic defects in bone growth and ectodermal organ formation. *Nat. Genet.* **24**, 391–395 (2000).
- Wilkie, A. O. M. et al. Functional haploinsufficiency of the human homeobox gene MSX2 causes defects in skull ossification. *Nat. Genet.* **24**, 387–390 (2000).
- Castaneda, B., et al. Role of RANKL (TNFSF11)-dependent osteopetrosis in the dental phenotype of Msx2 null mutant mice. *PLoS ONE* **8**, e80054 (2013).
- Xie, L. et al. Comparisons of gene expression between peripheral blood mononuclear cells and bone tissue in osteoporosis. *Medicine* **102**, E33829 (2023).
- Aïoub, M. et al. Msx2 $-/-$ transgenic mice develop compound amelogenesis imperfecta, dentinogenesis imperfecta and periodontal osteopetrosis. *Bone* **41**, 851–859 (2007).
- Tan, Z. et al. IRX3 and IRX5 inhibit adipogenic differentiation of hypertrophic chondrocytes and promote osteogenesis. *J. Bone Miner. Res.* **35**, 2444–2457 (2020).
- Wang, X. et al. UbiBrowser 2.0: a comprehensive resource for proteome-wide known and predicted ubiquitin ligase/deubiquitinase-substrate interactions in eukaryotic species. *Nucleic Acids Res.* **50**, D719–D728 (2022).
- Mishra, M. et al. FBW7 inhibits myeloid differentiation in acute myeloid Leukemia via GSK3-dependent ubiquitination of PU.1. *Mol. Cancer Res.* **19**, 261–273 (2021).
- Fukushima, H. et al. NOTCH2 Hajdu-Cheney mutations escape SCFFBW7-dependent proteolysis to promote osteoporosis. *Mol. Cell* **68**, 645–658.e5 (2017).
- Rodrigues, T., Reker, D., Schneider, P. & Schneider, G. Counting on natural products for drug design. *Nat. Chem.* **8**, 531–541 (2016).
- Ma, Q. et al. The SFRP1 inhibitor WAY-316606 attenuates osteoclastogenesis through dual modulation of canonical Wnt signaling. *J. Bone Miner. Res.* **37**, 152–166 (2022).
- Carey, H. A. et al. Enhancer variants reveal a conserved transcription factor network governed by PU.1 during osteoclast differentiation. *Bone Res.* **6**, 1–12 (2018).
- Lee, J. J. et al. Morusinol extracted from *Morus alba* inhibits arterial thrombosis and modulates platelet activation for the treatment of cardiovascular disease. *J. Atheroscler. Thromb.* **19**, 516–522 (2012).
- Kwon, H. W. Pharmacological actions of morusinol on modulation of platelet functions via integrin α IIb/ β 3 signaling. *J. Appl. Biol. Chem.* **66**, 171–178 (2023).
- Zelová, H. et al. Evaluation of anti-inflammatory activity of prenylated substances isolated from *Morus alba* and *Morus nigra*. *J. Nat. Prod.* **77**, 1297–1303 (2014).

37. Crotti, T. N. et al. PU.1 and NFATc1 mediate osteoclastic induction of the mouse $\beta 3$ integrin promoter. *J. Cell Physiol.* **215**, 636–644 (2008).
38. Holland, P. W. H., Booth, H. A. F. & Bruford, E. A. Classification and nomenclature of all human homeobox genes. *BMC Biol.* **5**, 1–28 (2007).
39. Takechi, M., Adachi, N., Hirai, T., Kuratani, S. & Kuraku, S. The Dlx genes as clues to vertebrate genomics and craniofacial evolution. *Semin Cell Dev. Biol.* **24**, 110–118 (2013).
40. Berdal, A. et al. Differential impact of Msx1 and Msx2 homeogenes on mouse maxillofacial skeleton. *Cells Tissues Organs.* **189**, 126–132 (2008).
41. Eyal, S. et al. Bone morphology is regulated modularly by global and regional genetic programs. *Dev. (Camb.)* **146**, 1–15 (2019).
42. Oono, F., Sakamoto, Y., Tachi, Y., Mabashi-Asazuma, H. & Iida, K. Effect of Cdx2 polymorphism on the relationship between dietary calcium intake and peak bone mass in young Japanese women. *Nutrients* **12**, 191 (2020).
43. Isaac, J. et al. DLX3 regulates bone mass by targeting genes supporting osteoblast differentiation and mineral homeostasis in vivo. *Cell Death Differ.* **21**, 1365–1376 (2014).
44. Kim, J. H. et al. Lhx2 regulates bone remodeling in mice by modulating RANKL signaling in osteoclasts. *Cell Death Differ.* **21**, 1613–1621 (2014).
45. Lézot, F. et al. Dlx homeobox gene family expression in osteoclasts. *J. Cell Physiol.* **223**, 779–787 (2010).
46. Jie, Z. et al. Activating, -catenin/Pax6 axis negatively regulates osteoclastogenesis by selectively inhibiting phosphorylation of p38/MAPK. *FASEB J.* **33**, 4236–4247 (2019).
47. Mirzayans, F., Lavy, R., Penner-Chea, J. & Berry, F. B. Initiation of early osteoblast differentiation events through the direct transcriptional regulation of Msx2 by FOXC1. *PLoS ONE* **7**, 1–8 (2012).
48. Ichida, F. et al. Reciprocal roles of Msx2 in regulation of osteoblast and adipocyte differentiation. *J. Biol. Chem.* **279**, 34015–34022 (2004).
49. Cheng, S. L., Shao, J. S., Cai, J., Sierra, O. L. & Towler, D. A. Msx2 exerts bone anabolism via canonical Wnt signaling. *J. Biol. Chem.* **283**, 20505–20522 (2008).
50. Sun, J., Ishii, M., Ting, M. C. & Maxson, R. Foxc1 controls the growth of the murine frontal bone rudiment by direct regulation of a Bmp response threshold of Msx2. *Development* **140**, 1034–1044 (2013).
51. Martin, T. J. & Sims, N. A. RANKL/OPG; Critical role in bone physiology. *Rev. Endocr. Metab. Disord.* **16**, 131–139 (2015).
52. Zhen, G. et al. An antibody against Siglec-15 promotes bone formation and fracture healing by increasing TRAP+ mononuclear cells and PDGF-BB secretion. *Bone Res.* **9**, 47 (2021).
53. Li, X. et al. Targeting actin-bundling protein L-plastin as an anabolic therapy for bone loss. *Sci. Adv.* **6**, 1–13 (2020).
54. Dou, C. et al. Sialylation of TLR2 initiates osteoclast fusion. *Bone Res.* **10**, 1–11 (2022).
55. Huang, T. et al. Targeting adipocyte ESRRA promotes osteogenesis and vascular formation in adipocyte-rich bone marrow. *Nat. Commun.* **15**, 1–20 (2024).
56. Kodama, J. & Kaito, T. Osteoclast multinucleation: review of current literature. *Int. J. Mol. Sci.* **21**, 1–35 (2020).
57. Izawa, N. et al. Cooperation of PU.1 with IRF8 and NFATc1 defines chromatin landscapes during RANKL-induced osteoclastogenesis. *J. Bone Miner. Res.* **34**, 1143–1154 (2019).
58. de la Rica, L. et al. PU.1 target genes undergo Tet2-coupled demethylation and DNMT3b-mediated methylation in monocyte-to-osteoclast differentiation. *Genome Biol.* **14**, 1–21 (2013).
59. Doble, B. W. & Woodgett, J. R. GSK-3: tricks of the trade for a multi-tasking kinase. *J. Cell Sci.* **116**, 1175–1186 (2003).
60. Davis, R. J., Welcker, M. & Clurman, B. E. Tumor suppression by the Fbw7Ubiquitin ligase: mechanisms and opportunities. *Cancer Cell* **26**, 455–464 (2014).
61. Ramchand, S. K. & Leder, B. Z. Sequential therapy for the long-term treatment of postmenopausal osteoporosis. *J. Clin. Endocrinol. Metab.* 1–9, <https://doi.org/10.1210/clinem/dgad496> (2023).
62. Langdahl, B. L. et al. Romosozumab (sclerostin monoclonal antibody) versus teriparatide in postmenopausal women with osteoporosis transitioning from oral bisphosphonate therapy: a randomised, open-label, phase 3 trial. *Lancet.* **390**, 1585–1594 (2017).
63. Wang, Y. et al. The hypoxia-inducible factor α pathway couples angiogenesis to osteogenesis during skeletal development. *J. Clin. Investig.* **117**, 1616–1626 (2007).
64. Duvall, C. L., Taylor, W. R., Weiss, D. & Guldberg, R. E. Quantitative microcomputed tomography analysis of collateral vessel development after ischemic injury. *Am. J. Physiol. Heart Circ. Physiol.* **287**, 302–310 (2004).
65. Recker, R. R. et al. Issues in modern bone histomorphometry. *Bone* **49**, 955–964 (2011).
66. Wang, S. et al. An antioxidant sesquiterpene inhibits osteoclastogenesis via blocking IPMK/TRAF6 and counteracts OVX-induced osteoporosis in mice. *J. Bone Miner. Res.* **36**, 1850–1865 (2021).
67. Dou, C. et al. Graphene-based microRNA transfection blocks pre-osteoclast fusion to increase bone formation and vascularization. *Adv. Sci.* **5**, 1–10 (2018).
68. Huang, J. et al. Harmine enhances type H vessel formation and prevents bone loss in ovariectomized mice. *Theranostics* **8**, 2435–2446 (2018).
69. Jumper, J. et al. Highly accurate protein structure prediction with AlphaFold. *Nature* **596**, 583–589 (2021).
70. Hodsdon, M. E., Ponder, J. W. & Cistola, D. P. The NMR solution structure of intestinal fatty acid-binding protein complexed with palmitate: application of a novel distance geometry algorithm. *J. Mol. Biol.* **264**, 585–602 (1996).
71. Muzzammel, H. et al. Identification of RdRp inhibitors against SARS-CoV-2 through E-pharmacophore-based virtual screening, molecular docking and MD simulations approaches. *Int. J. Biol. Macromol.* **237**, 1–10 (2023).
72. Sahin, K. In silico identification of angiotensin-1 converting enzyme inhibitors using text mining and virtual screening. *J. Biomol. Struct. Dyn.* **40**, 1152–1162 (2022).

Acknowledgements

This work was supported by the National Natural Science Foundation of China (82002334, 82372440), The Key Project of National Natural Science Foundation of China (82330077), Union Fund Project of National Natural Science Foundation of China (U21A20351), and Natural Science Foundation of Zhejiang Province (Q20H060042, LQ24H090007, LQN25H070001).

Author contributions

Q.M., S.F., Z.X., and Z.J. conceived the study. S.W., H.X. (Hong Xue), L.N., P.Y., Y.S., and J.Z. performed most of the experiments. Q.M., H.W., and H.X. (Hongwei Xie) performed the bioinformatic analysis. B.Z., Q.W., and C.J. provided experimental assistance. Q.M., Z.J., and S.W. oversaw the collection of results and data interpretation. Q.M. and Z.J. wrote the manuscript. A.Q., S.F., L.N., and Z.X. contributed ideas and reviewed the manuscript. All authors have seen and approved the final version of the paper.

Competing interests

The authors declare no competing interests.

Additional information

Supplementary information The online version contains supplementary material available at <https://doi.org/10.1038/s41467-025-61938-0>.

Correspondence and requests for materials should be addressed to Shunwu Fan, Ziang Xie or Zhiwei Jie.

Peer review information *Nature Communications* thanks the anonymous reviewer(s) for their contribution to the peer review of this work. A peer review file is available.

Reprints and permissions information is available at <http://www.nature.com/reprints>

Publisher's note Springer Nature remains neutral with regard to jurisdictional claims in published maps and institutional affiliations.

Open Access This article is licensed under a Creative Commons Attribution-NonCommercial-NoDerivatives 4.0 International License, which permits any non-commercial use, sharing, distribution and reproduction in any medium or format, as long as you give appropriate credit to the original author(s) and the source, provide a link to the Creative Commons licence, and indicate if you modified the licensed material. You do not have permission under this licence to share adapted material derived from this article or parts of it. The images or other third party material in this article are included in the article's Creative Commons licence, unless indicated otherwise in a credit line to the material. If material is not included in the article's Creative Commons licence and your intended use is not permitted by statutory regulation or exceeds the permitted use, you will need to obtain permission directly from the copyright holder. To view a copy of this licence, visit <http://creativecommons.org/licenses/by-nc-nd/4.0/>.

© The Author(s) 2025